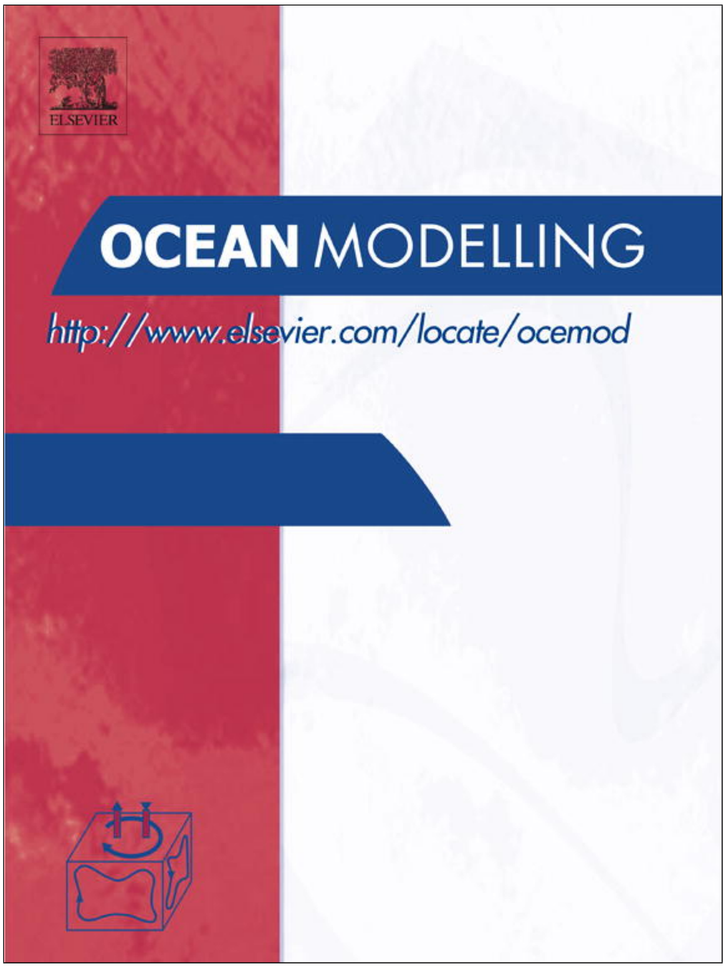
ELSEVIER
OCEAN MODELLING
http://www.elsevier.com/locate/ocemod

Ocean Modelling 64 (2013) 29–45

Contents lists available at SciVerse ScienceDirect

Ocean Modelling

journal homepage: www.elsevier.com/locate/ocemod

An Ensemble Kalman Filter multi-tracer assimilation: Determining uncertain ocean model parameters for improved climate-carbon cycle projections

M. Gerber *, F. Joos

Climate and Environmental Physics, Physics Institute, University of Bern, 3012 Bern, Switzerland
Oeschger Centre for Climate Change Research, University of Bern, Switzerland

A R T I C L E I N F O

Article history:
Received 12 April 2012
Received in revised form 16 December 2012
Accepted 18 December 2012
Available online 20 January 2013

Keywords:
Ensemble Kalman Filter
Multi tracer assimilation
Ocean model parameter

A B S T R A C T

An Ensemble Kalman Filter is applied to assimilate observed tracer fields in various combinations in the Bern3D ocean model. Each tracer combination yields a set of optimal transport parameter values that are used in projections with prescribed CO_2 stabilization pathways. The assimilation of temperature and salinity fields yields a too vigorous ventilation of the thermocline and the deep ocean, whereas the inclusion of CFC-11 and radiocarbon improves the representation of physical and biogeochemical tracers and of ventilation time scales. Projected peak uptake rates and cumulative uptake of CO_2 by the ocean are around 20% lower for the parameters determined with CFC-11 and radiocarbon as additional target compared to those with salinity and temperature only. Higher surface temperature changes are simulated in the Greenland–Norwegian–Iceland Sea and in the Southern Ocean when CFC-11 is included in the Ensemble Kalman model tuning. These findings highlights the importance of ocean transport calibration for the design of near-term and long-term CO_2 emission mitigation strategies and for climate projections.

1. Introduction

A quantitative understanding of surface-to-deep transport rates of anthropogenic carbon and heat in the ocean is a prerequisite for reliable projections of future atmospheric CO_2, ocean acidification, sea level rise and global climate change and to design reliable carbon emission mitigation strategies. However, projections are still hampered by uncertainties related to limited capabilities to model ocean transport (Cao et al., 2009; Schmittner et al., 2009; Plattner et al., 2008). In contrast to weather forecast or seasonal-to-decadal prediction, decadal-to-millennial scale carbon cycle-climate projections only weakly depend on initial conditions, but do depend on the choice of model parameters that determine physical transport rates. It is standard to systematically tune transport parameters in simplified box models towards the observed gradients in ventilation time scale tracers such as radiocarbon and CFC-11 (e.g. Revelle and Suess, 1957; Oeschger et al., 1975; Joos et al., 1991). On the other hand, the complexity and computing requirements of more comprehensive Earth System models have generally prevented the determination of model parameters in a systematic way.

The goals of this study are (i) to determine optimal model parameters by assimilating temperature, salinity, CFC-11 and radiocarbon fields in the Bern3D dynamic ocean model using an Ensemble Kalman Filter as a statistical framework to best fit the observations available, and (ii) to investigate whether ventilation time scale tracers such as CFC-11 and radiocarbon provide additional information compared to temperature and salinity and whether this is relevant for the representation of biogeochemical tracers and climate projections.

A particular important parameter in ocean circulation models is the diapycnal (or vertical) diffusivity coefficient, k_{dia} (Bryan, 1987). k_{dia} strongly influences the rate of ocean overturning by influencing the balance of diffusive and advective heat transport into the deep (Munk, 1966). There are additional parameters that can also exert significant influences such as those related to friction, eddy induced transport in region of sloping isopyncals such as the Southern Ocean (Gent et al., 1995) and mixing along isopycnals.

Data assimilation and probabilistic approaches are applied in a range of studies to determine ocean parameters of Earth System Models of Intermediate Complexity (EMIC) or of spatially-resolved ocean models (e.g., Schlitzer, 2000, 2002; Hargreaves et al., 2004; Schmittner et al., 2009). Schlitzer (2007) applied an adjoint approach to determine time-invariant, annual mean velocities and mixing coefficients as well as biogeochemical fluxes and to place constraints on bottom water formation rates using observation-based distribution of temperature, salinity, CFC-11, radiocarbon and biogeochemical tracers as target. Hargreaves et al. (2004) relying on previous work of Annan et al. (2005), applied an Ensemble Kalman Filter (EnKF) (Evensen, 2003) to assimilate ocean temperature and salinity fields as well as surface air-temperature and

* Corresponding author at: Climate and Environmental Physics, Physics Institute, University of Bern, 3012 Bern, Switzerland. Tel.: +41 31 631 4464; fax: +41 31 631 8742.
E-mail address: mgerber@climate.unibe.ch (M. Gerber).

1463-5003/$ - see front matter © 2013 Elsevier Ltd. All rights reserved.
http://dx.doi.org/10.1016/j.ocemod.2012.12.012

humidity fields into their EMIC to determine optimal parameter values. These were then used to project changes in the Atlantic Meridional Overturning Circulation (AMOC) under prescribed anthropogenic forcing. No tracer with explicit information on ventilation time scales such as CFC-11 or radiocarbon was included. Schmittner et al. (2009) applied a Bayesian data-model fusion method to determine a single parameter, the diapycnal diffusivity coefficient, relying on 8 model simulations and using the distributions of a range of physical and biogeochemical ocean tracers including CFC-11 and radiocarbon as target. They constrain the diapycnal diffusivity in the pelagic pycnocline to be around 0.5–$2.0 \times 10^{-5}\,m^2\,s^{-1}$ in their model, thereby confirming a previous finding of Müller et al. (2006). These authors find a diapycnal diffusivity coefficient of $1.0 \times 10^{-5}\,m^2\,s^{-1}$ to fit best with observation-based CFC-11 inventories and radiocarbon signatures of the main deep water masses (Matsumoto et al., 2004). Bhat et al. (2012) relied on the same model output as Schmittner et al. (2009) and utilized CFC-11 and radiocarbon fields to further constrain the diapycnal diffusivity parameter. Goes et al. (2010) applied a similar Baysian approach relying on horizontally averaged profiles of temperature, CFC-11, and radiocarbon to determine the background diapycnal diffusivity and a Southern Ocean mixing parameter.

These earlier studies may suffer from potential shortcomings. These include the determination of time-invariant velocities, the neglect of ventilation time scale tracers in the assimilation or the determination of one or two parameters only. It appears therefore timely to assimilate multiple, spatially-resolved 3-dimensional tracer fields into a dynamic ocean model to determine a suite of relevant ocean model parameters and to apply the optimal parameter solutions in climate-carbon cycle projections as is the purpose of this study.

Previous studies show that model differences in deep ocean mixing and transport contribute substantially to the wide range of ocean heat (Gregory and Mitchell, 1997; Russell et al., 2006; Boé et al., 2009) and carbon uptake (Joos et al., 1999; Friedlingstein et al., 2003) in anthropogenic climate change projections and that tracer distributions depend sensitively on ocean circulation and transport (England and Maier-Reimer, 2001; Doney et al., 2004; Matsumoto et al., 2004; Najjar et al., 2007). Another novel aspect of our work is that we address these uncertainties by assimilating different combinations of observation-based fields.

Our approach is as follows. An Ensemble Kalman Filter (EnKF) assimilation is applied to determine the optimal parameters of the Bern3D coarse resolution, 3-dimensional dynamic ocean circulation model. The EnKF (Evensen, 2003) is a well-established technique and has, for example been used to estimate the distribution of nitrate and zooplankton by assimilating chlorophyll data (Natvik and Evensen, 2003), to estimate the distribution of sea-ice (Lisæter et al., 2003), and to infer air–sea fluxes of natural and anthropogenic carbon (Gerber et al., 2009; Gerber and Joos, 2010). Global gridded fields of temperature and salinity (Locarnini et al., 2010; Antonov et al., 2010) are assimilated in a first experiment. CFC-11 (Key et al., 2004) is included as a third tracer in a second experiment and the modern radiocarbon distribution (Key et al., 2004) as a fourth field in the third experiment. The performance of the different setups is evaluated in terms of their ability to simulate observed tracer fields. The optimal parameters are used in long-term climate-carbon cycle projections where the CO_2 stabilization profiles SP450 and SP1000 with stabilization at 450 and 1000 ppm are prescribed over the period 1765 to year 3000 AD. Unlike many earlier studies that addressed long term climate stabilization (e.g., Joos et al., 1999; Plattner et al., 2008; Frölicher and Joos, 2010), we also include an ocean sediment module in our model setup.

A shortcoming of this study is the coarse spatial resolution (36 by 36 grid cells by 32 vertical layers) of the current Bern3D version. This leads to problems with regard to the representation of intermediate waters and the strength of the subpolar and subtropical gyres and the Antarctic Circumpolar Current. The goal here is then not to reconstruct spatio-temporal details of the ocean circulation, but to optimize basin scale overturning and surface-to-deep transport time scales. Surface-to-deep transport is the rate limiting step for the uptake of anthropogenic carbon by the ocean.

Our novel data assimilation and modeling strategy yields new insight. First, the inclusion of the tracers CFC-11 and radiocarbon in the assimilation appears to improve the representation of ocean ventilation and the large-scale distribution of ventilation time scale tracers and biogeochemical tracers. Second, the peak uptake rates of CO_2 by the ocean are about 27% lower for these parameter sets compared to the set obtained from temperature and salinity fields. Cumulative uptake of anthropogenic carbon is also about 26% lower by year 3000 AD. This points to the usefulness of assimilating CFC-11 and radiocarbon data to improve near-term CO_2 emission mitigation strategies as well as to define total allowable carbon emissions to meet a certain temperature target (Meinshausen et al., 2009).

2. Method

2.1. Model setup

2.1.1. The Bern3D ocean model

The Bern3D ocean model (Müller et al., 2006) is a frictional-geostrophic balance dynamic ocean model with a horizontal resolution of 36×36 (horizontal) grid cells. The 32 layers increase in thickness from 38 m at the surface to 397 m at depth. The physical core is based on the ocean model of Edwards and Marsh (2005), but has been modified to include more layers, a semi-implicit numerical scheme to solve the vertical diffusion–advection equation using the diffusive parameterization of the eddy-induced transport following Griffies (1998), and to distinguish the parameters for diapycnal and Gent–McWilliams mixing. It has also been coupled with an energy balance atmosphere (Ritz et al., 2011), a sediment module (Tschumi et al., 2011), and a marine ecosystem module (Gangstø et al., 2011). For the EnKF assimilation, the stand-alone ocean version is applied in a configuration including additional freshwater fluxes into the North Atlantic and into the Weddell Sea as well as an open Bering strait and Indonesian Passage as introduced by Ritz et al. (2011).

The marine biogeochemical cycle model is fully coupled to the physical ocean model (Parekh et al., 2008; Tschumi et al., 2008). The prognostic state variables considered in the model are dissolved inorganic carbon (DIC), total alkalinity, ^{13}C, ^{14}C, phosphates (PO_4^{3-}), dissolved organic carbon, oxygen, silica and iron. New production is a function of temperature, light, phosphate and iron following Doney et al. (1996) and remineralisation of particulate organic matters follows a prescribed depth profile according to a power law scaling. The competition between opal and calcite producers is modeled following the formulations of the HAMOCC5 model of Maier-Reimer et al. (2005). The sedimentary component (Tschumi et al., 2011) represents sediment formation, redissolution, remineralization as well as sediment diagenesis in the top 10 cm beneath the seafloor in the pelagic ocean and the accumulation of opal, $CaCO_3$ and organic matter (Heinze et al., 1999; Gehlen et al., 2006).

The coarse resolution of the Bern3D ocean model and the fast integration time makes it well suited for paleoclimate studies and ensemble simulations which requires a lot of computational time. The model is able to represent the broad scale ocean circulation, despite its coarse resolution. Shortcomings of the standard model setup include a too weak Antarctic Bottom Water formation, a too deep North Atlantic Deep Water formation, a weak gyre circulation and a weak Antarctic Circumpolar Current.

For spin-up, seasonal surface fields for temperature and salinity and wind stress (Levitus and Boyer, 1994; Levitus et al., 1994; Kalnay et al., 1996) are prescribed for 5000 years and the average air-sea freshwater fluxes diagnosed during the last 100 years of this first phase; then, the model is switched to mixed-boundary conditions and forced with diagnosed freshwater fluxes instead of with salinity fields. An additional freshwater flux (f_w) is applied in the northern North Atlantic to mimic moisture transport from the Pacific to the Atlantic and to promote the formation of North Atlantic Deep Water. A preindustrial near steady state is reached after 5000 years of mixed forcing. The reconstructed evolution of atmospheric Δ^{14}C and of CFC-11 is prescribed from year 1770 AD to present. The formulation of the gasexchange of CFC-11 and Δ^{14}C is described in Müller et al. (2006); the rate depends quadratically on wind speed and global mean transfer rate is reduced by 19% compared to earlier studies (Wanninkhof, 1992) in order to find good agreement of simulated quantities with a range of data-based metrics. The spinup is performed with a constant 0‰ Δ^{14}C atmosphere.

The parameters (Table 1) of the standard setup (STD) were hand-tuned (Müller et al., 2006) towards five targets: the inventories of CFC-11 in the Pacific and Indian Oceans north of 40°S and the Indo-Pacific sector of the Southern Ocean (south of 40°S) and the mean radiocarbon signature of North Atlantic, North Pacific, and Circumpolar Deep Water (Matsumoto et al., 2004). Model parameters include the diffusion coefficient for diffusive transport along isopycnal surfaces (K_{iso}) and across isopycnal surfaces (K_{dia}); the Gent–McWilliams mixing parameter (κ_{GM}) for eddy-induced transport (Gent et al., 1995; Griffies, 1998), and parameters scaling friction (λ), the above described freshwater flux into the northern North Atlantic (f_w), and wind stress scaling (*windscale*). The friction scaling parameter (λ) is implemented to suppress numerical instabilities related to pseudo-Kelvin waves (Edwards and Marsh, 2005). The wind stress scaling (*windscale*) is introduced to enhance the strength of the wind-driven gyres (Edwards and Marsh, 2005).

The standard way to calculate radiocarbon signatures in the Bern3D model is to include a marine biogeochemical module (Tschumi et al., 2011). Dissolved inorganic and organic carbon (DIC, DOC) and radiocarbon (DIC-14, DOC14) are included as tracers along with other required biogeochemical tracers such as alkalinity, iron, and phosphate. The transport of all these tracers imposes a computational burden. Fortunately, the procedure can be simplified by transporting instead only one tracer, the fractionation corrected ^{14}C/^{12}C ratio of DIC, ^{14}R. This is an approximation as the variations of DIC within the ocean are of order 10% and all biological mediated fluxes and reservoirs as well as ocean-sediment interactions are neglected. We apply a first order correction to minimize this bias. For this, the Δ^{14}C distribution was computed from DIC and DIC-14 with the marine biogeochemical module and ocean sediments included as well as from the tracer ^{14}R and with standard model parameters. The difference between the two Δ^{14}C fields is used in all simulations to correct the modeled ^{14}R fields. This correction is in the range of 0–30‰ and thus relatively small compared to the overall Δ^{14}C range of order 300‰. The formulation of the ^{14}R is described in Müller et al. (2006).

Table 1
Optimized parameters from different EnKF-data assimilations. In EXP1, observation-based seasonal temperature (T) and salinity (S) fields are assimilated into the Bern3D model. In EXP2, observation-based T, S, and CFC-11 fields and in EXP3 observation-based T, S, CFC-11 and $\Delta^{14}C$ fields are assimilated. The STD setup (Müller et al., 2006; Ritz et al., 2011) was tuned towards inventories of CFC-11 and $\Delta^{14}C$ as proposed in Matsumoto et al. (2004).

Parameter	EXP1	EXP2	EXP3	STD
κ_{GM} (m^2 s^{-1})	4866	4206	3841	2000
K_{dia} (m^2 s^{-1})	$3.7 \cdot 10^{-5}$	$3.82 \cdot 10^{-5}$	$1.74 \cdot 10^{-5}$	$1 \cdot 10^{-5}$
Wind scale	3.01	1.82	2.40	2
λ	2.8	3.01	2.23	2
K_{iso} (m^2 s^{-1})	3003	3415	3287	1000
f_w (Sverdrup)	0.173	0.172	0.179	0.17

2.2. Ensemble Kalman Filter multi tracer data assimilation

2.2.1. Optimization scheme

The EnKF is a sequential filter method to estimate unknown model states or parameters by assimilating data into the model as described in depth in Evensen (2003). An ensemble of models is run forward in time and whenever observations are available they are used to update the model states or parameters before the integration of the ensemble proceeds on. We chose a parameter forecast ψ_i^f for each ensemble member $i \in (1, \ldots, N = 64)$. ψ_i^f includes a set of n physical parameters of the Bern3D ocean model (Table 1) which are iteratively optimized.

For each ensemble member, a model with its set of six physical parameters is run towards a preindustrial steady state and over the industrial period. Modeled temperature and salinity fields are sampled for the preindustrial state whereas CFC-11 and $\Delta^{14}C$ values are sampled from the model at the time when observations for a specific grid cell are available. Afterward, the ensemble members are then updated in the EnKF optimization scheme. We use the formulation of the EnKF proposed in Evensen (2003). The analyzed parameters (the ensemble member after the optimization step) ψ^a are written as:

$$\psi^a = \psi^f + K(D - H\psi^f) \tag{1}$$

where K denotes the Kalman gain, ψ^f is the parameter forecast (the ensemble member prior to the optimization step), H is the measurement operator linking the "true", unknown parameter to the data: $H\psi^t = d + \epsilon$. $D = (d_1, \ldots, d_N)$ is the matrix holding the measurement vectors d_i which consist of the observations d plus an error ϵ_i, $d_i = d + \epsilon_i$ assuming that the measurement vectors d_i are normally distributed around the observation d.

In our study, d_i includes measurements of CFC-11, T, S and $\Delta^{14}C$, respectively. $H\psi^t$ are the corresponding modeled fields. The error of each tracer field is randomly generated assuming Gaussian error distribution with prescribed standard deviations for the temperature, salinity, CFC-11, and $\Delta^{14}C$ data. For each tracer, we set these standard deviations to be equal to ±5% of the standard deviation of all available data. This yields 0.32 °C for temperature, 0.027 psu in salinity, 5‰ in $\Delta^{14}C$ and 6.3×10^{-11} mol/m^3 (=0.0615 pmol/kg) for CFC-11. An experiment including a vertical structure of the T and S errors has provided very similar results as when assuming constant errors.

The Kalman gain K is computed from the ensemble covariance P^f, and the measurement error covariance R. A solution for the Kalman gain can be written following Evensen (2003):

$$K = P^f H^T (HP^f H^T + R)^{-1} \tag{2}$$

The ensemble covariance P^f can be obtained by approximating the "true" model parameter ψ^t with the ensemble mean. The ensemble covariance then reads:

$$P = \overline{(\psi^f - \bar{\psi}^f)(\psi^f - \bar{\psi}^f)^T} \tag{3}$$

The overline denotes the expectation values. The ensemble covariance has dimension $n \times n$, the error covariance R (dimension $m \times m$, m being the number of observations) is $\propto (\epsilon_1, \ldots, \epsilon_N)(\epsilon_1, \ldots, \epsilon_N)^T$ with above described errors ϵ_i. The algorithm proposed in Evensen (2003) does not require an explicit formulation of the measurement operator H (dimension $m \times n$, m being the number of observations and n the number of optimized parameters), instead modeled output fields from the Bern3D model and the above described measurement error covariance matrix are use to compute the Kalman-Gain, as all properties of the Kalman-Gain can be expressed in terms of $H\psi^f$ and R. For further detail we refer to Evensen (2003).

2.2.2. Data and experiments

We use seasonal temperature and salinity fields from the World Ocean Atlas 2009 (WOA 2009) climatology (Locarnini et al., 2010; Antonov et al., 2010). The CFC-11 and $\Delta^{14}C$ data are station data from the GLODAP data base (Key et al., 2004). Each station data point is interpolated to the appropriate grid cell and is regarded as annual mean value of the corresponding year of collection. We use CFC-11 data from the years 1991 to 1996 and $\Delta^{14}C$ from the years 1972 to 1997. In other words, the radiocarbon signal from the atomic bomb tests and from fossil fuel is included.

We run three experiments to explore the influence of different tracers on the solution and to investigate whether the inclusion of additional tracers in the assimilation provides additional information. In the first experiment (EXP1), we only assimilate temperature and salinity fields, in the second (EXP2), we assimilate temperature, salinity and CFC-11 and in the third experiment (EXP3) we assimilate temperature, salinity, CFC-11 and $\Delta^{14}C$. The initial ensemble has been perturbed around the standard solution of the Bern3D model as reported in Müller et al. (2006) and Ritz et al. (2011). The optimization is run until convergence of the parameter; here we use the convergence of the average of all tracer-assimilations, which is typically reached after a few iteration steps.

3. Results

3.1. Optimal parameter solutions for different assimilation targets and their influence on simulated circulation, temperature, salinity, CFC-11, and $\Delta^{14}C$

Each of the three assimilation experiments as well as the standard setup produces a different set of optimized parameter (see Table 1), which each yields a different ocean circulation (Fig. 1) and different tracer distributions. In Figs. 2–5, we plot the difference between simulated and observed values for all four tracers. The observations are shown in Figs. 6 and 7. At first glance, the difference plots appear difficult to interpret. However, a consistent picture emerges when comparing differences with observations and the streamfunction of Fig. 1. All four setups share common shortcomings which are evidenced by similar features in the differences between modeled and observed tracer fields. These are briefly discussed in the following paragraphs, before turning to the specifics of the individual setups.

The formation of intermediate water masses and their equatorwards propagation is generally too weak in all four setups. The exchange of subtropical and equatorial surface waters with the thermocline tends to be too vigorous and the thermocline too diffusive which results in too weak vertical tracer gradients. This is for example evidenced by too low CFC-11 concentrations around 50°S and around 35° N in the Atlantic and Pacific and too high CFC-11 concentration in the low-latitude thermocline of the Pacific and North Atlantic. The tongues of fresh waters in the Pacific and South Atlantic and of salty water in the North Atlantic thermocline are not expressed as well as observed again pointing to too weak formation rates of intermediate waters. On the other hand, ventilation of the thermocline in the northern North Pacific is too rapid as evidenced by too high CFC-11 concentrations and $\Delta^{14}C$.

The deep Pacific tends to be ventilated to rapidly as evidenced by higher than observed $\Delta^{14}C$ and a cold bias, whereas North Atlantic Deep Water has a tendency to penetrate too deep and Antarctic Bottom Water formation is too weak. The deep Atlantic tends to be too warm and there is a tendency towards too high radiocarbon signatures in the very deep South Atlantic.

The performance of the standard setup of the Bern3D ocean model was compared to other models in earlier studies. The skill of the Bern3D model in representing the observation-based radiocarbon distribution compares with a score of 0.93 favorably to that of general circulation ocean models with a range of skill scores from 0.65 to 0.94 (Mikaloff Fletcher et al., 2007). The skill score used in Mikaloff Fletcher et al. (2007) is described in Taylor (2001) and values were computed by comparing bottle data with appropriate grid cell values (without interpolation). Müller et al. (2006) find root-mean-square differences between modeled and observation-based (Levitus and Boyer, 1994; Levitus et al., 1994) annual mean values of 1.0 °C for temperature and 0.20 psu for salinity, well within the ranges of 0.8–2.7 °C and 0.15–0.31 psu of the other prognostic models used in the Ocean Model Intercomparison Project (Najjar et al., 2007). The root-mean-square-error (rmse), relative standard deviation, and correlation coefficient between a simulated and observation-based field are given in Table 2 for all four model setups.

The assimilation of temperature and salinity in EXP1 yields higher values of the Gent–McWilliams, isopycnal and diapycnal diffusivity parameters, the inverse drag, and the wind stress

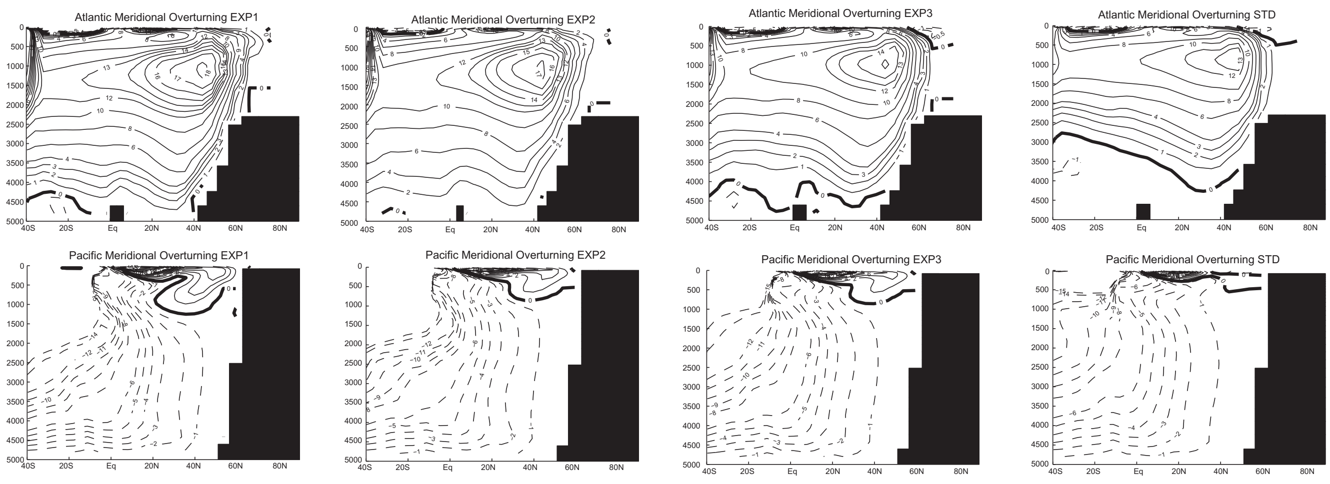

Fig. 1. Atlantic- and Pacific overturning streamfunction in Sverdrup for the three EnKF circulation setups (EXP1, EXP2 and EXP3) and for the standard circulation setup (STD).

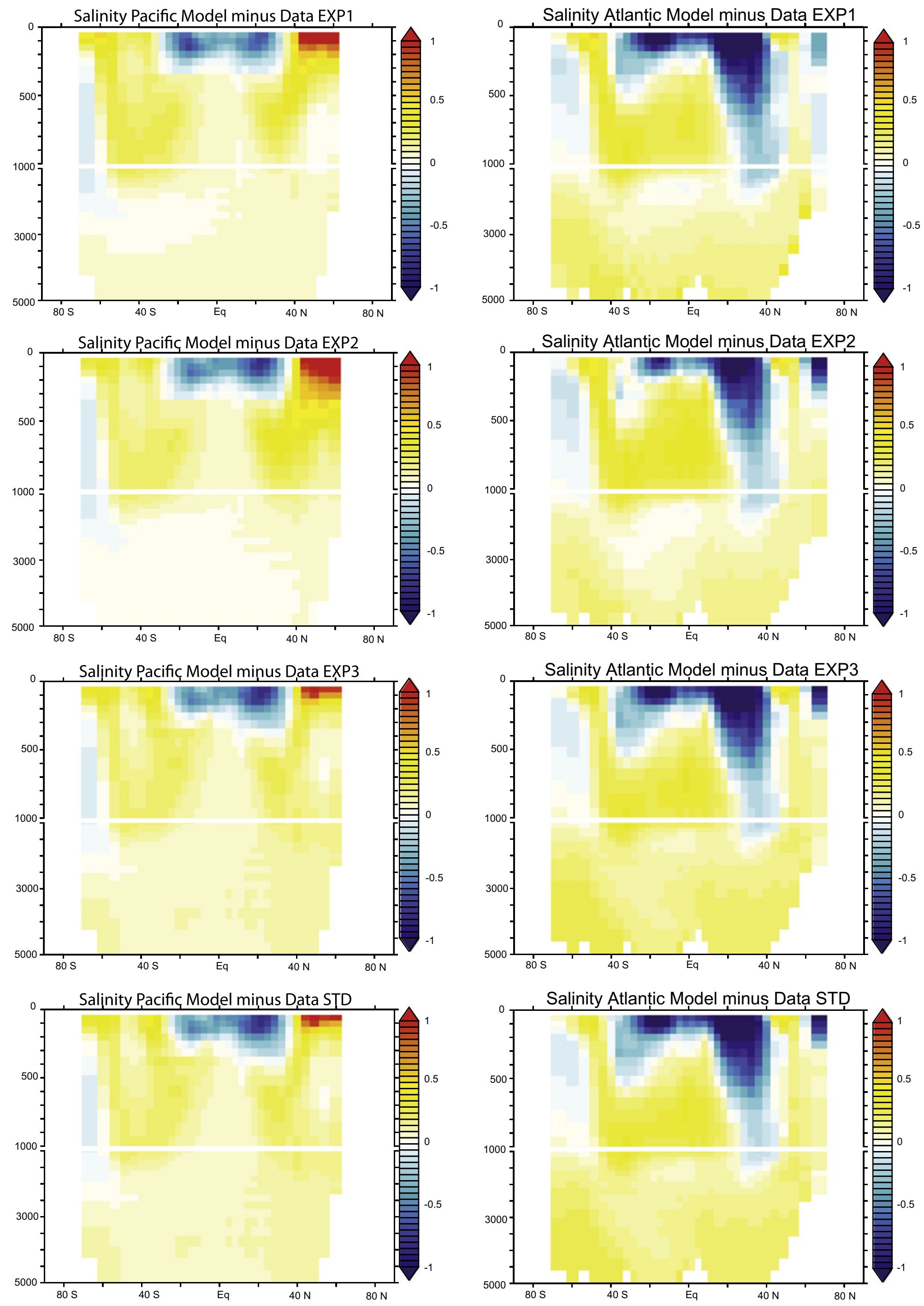

Fig. 2. Summer (JJA) salinity residuals (model minus data in psu) in the Pacific and Atlantic for the three EnKF- and the standard circulation setups.

scaling parameters compared to the standard setup (Table 1). This causes a stronger overturning in the Southern Ocean and a stronger formation and deeper penetration of the North Atlantic Deep Water (NADW) and higher upwelling through enhanced Ekman transport than in the standard setup. The NADW strength of 18 Sv compares well with data-based estimates (Ganachaud and Wunsch, 2000), however it penetrates too deep and Antarctic Bottom Water (AABW) does hardly enter the North Atlantic. The diapycnal diffusivity coefficient is with $3.7 \cdot 10^{-5}\,m^2\,s^{-1}$, higher than the estimate of $0.5–2 \cdot 10^{-5}\,m^2\,s^{-1}$ of Schmittner et al. (2009) and as the estimate for the standard setup ($1.0 \cdot 10^{-5}\,m^2\,s^{-1}$) Müller et al. (2006).

The revised parameters of EXP1 largely remove the cold bias in the deep Pacific, but increase the warm bias in the equatorial thermocline of the Atlantic and Pacific. The ventilation of the equatorial thermocline is now too vigorous as evidenced by too high CFC-11 concentrations in the low latitude thermocline of the Atlantic and Pacific (Fig. 4). Similarly, ventilation of the deep Pacific and of the bottom water in the Atlantic is too rapid and $\Delta^{14}C$ is biased high below 500 m in the Pacific and below 3500 m in the Atlantic. The low bias in $\Delta^{14}C$ in the upper Pacific is likely linked to too much upwelling of old, $\Delta^{14}C$ poor waters from depth.

The observed temperature distribution is in relative terms better reproduced than the salinity distribution in EXP1. The

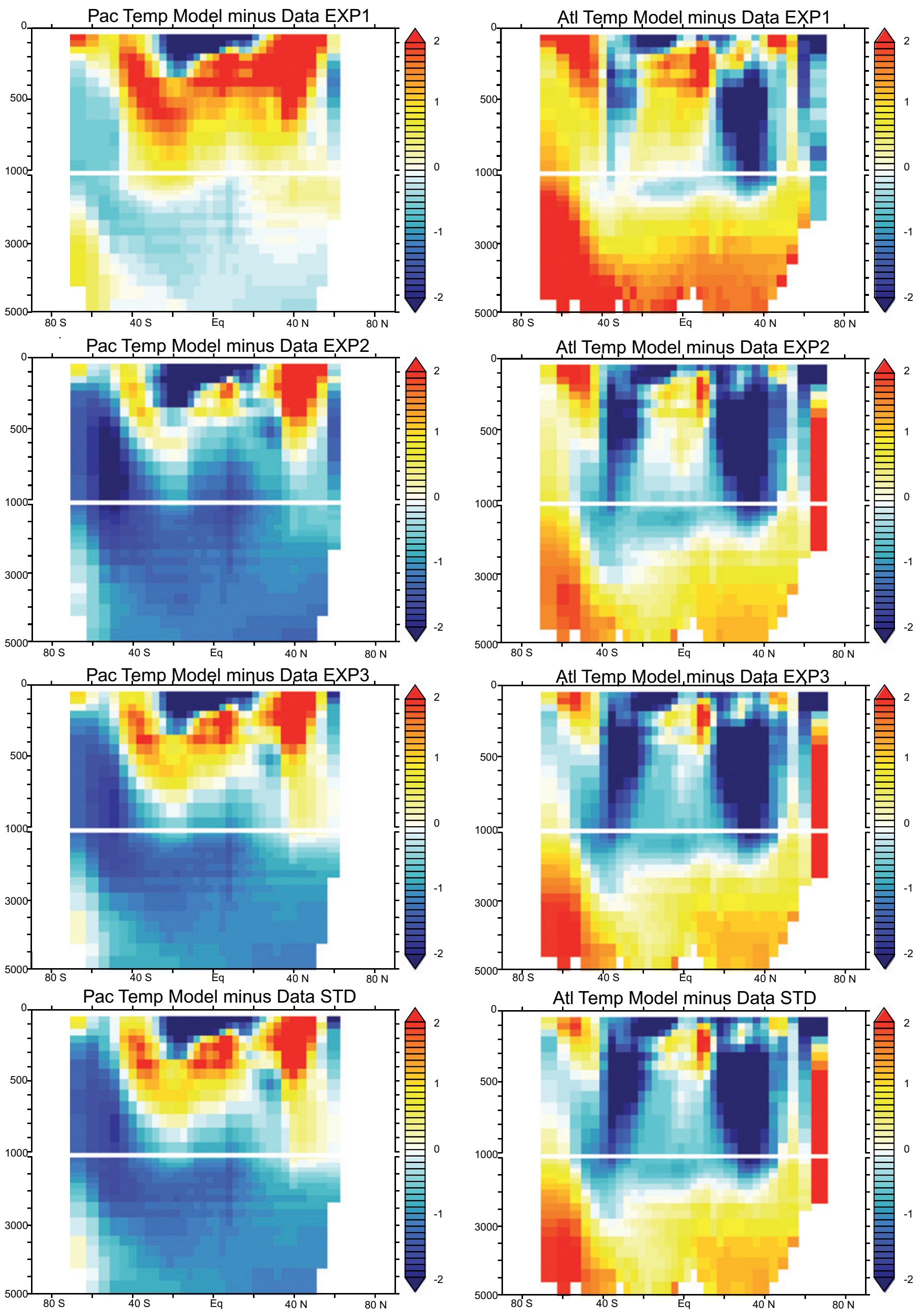

Fig. 3. Summer (JJA) temperature residuals (model minus data, in °C) in the Pacific and Atlantic for the three EnKF- and the standard circulation setups.

root-mean-square-error (rmse) of simulated temperature with respect to the observations is about 30% of the standard deviation of the latter, whereas the corresponding rmse of the salinity field is about 78%. In absolute units, the rmse is 1.78 °C for temperature and 0.35 for salinity data. We note that these deviations are obtained from seasonal data and by giving equal weight to each grid cell.

In conclusions, the results of EXP1, where only temperature and salinity fields were used to determine parameters in the EnKF assimilation, suggest that transport of heat, radiocarbon and CFC-11 from the surface to the thermocline is too vigorous and that the deep Pacific is ventilated too rapidly.

In a next step, we include CFC-11 in the EnKF assimilation. We do expect somewhat more realistic surface-to-thermocline transport rates in EXP2 compared to EXP1. CFC-11 observations provide information about the mixing time scales of the upper ocean. The higher the surface-to-deep transport, the higher the CFC-11 concentrations in the thermocline. The solubility of CFC-11 and thus CFC-11 concentrations do also depend on temperature. However, deviations in modeled temperature of order 1 °C are too small to be relevant in this context.

The additional assimilation of CFC-11 in EXP2 reduces the wind scaling parameter by about 40% and the Gent–McWilliams mixing parameter by 13% (Table 1) compared to EXP1. In turn, the vigorous surface-to-deep exchange around Antarctica and in the northern North Pacific is somewhat reduced. On the other hand, the diapycnal diffusivity parameter and the freshwater flux in the North Atlantic are similar in EXP1 and EXP2 (Table 1) and so is the formation and penetration of NADW (Fig. 1). The inclusion of CFC does not improve the representation of NADW as CFC concentrations are low in NADW away from its source region.

The addition of a third tracer, CFC-11, to the assimilation reduces the weight for salinity and temperature. Not surprisingly

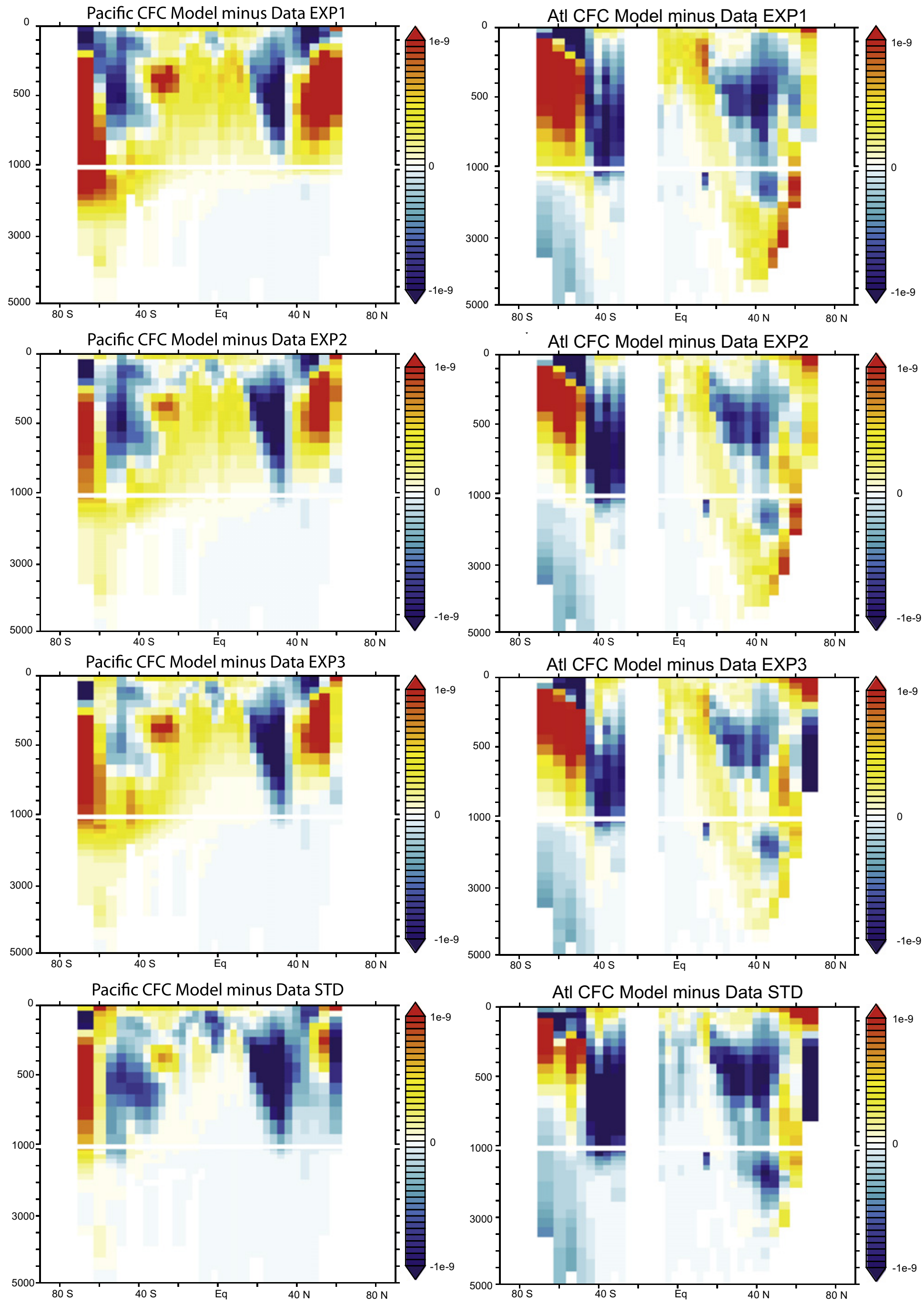

Fig. 4. CFC-11 residuals (model minus data, in mol m^{-3}) in the Pacific and Atlantic for the year 1993.

then, the rmse of salinity is increased from 0.35 in EXP1 to 0.38 in EXP2. On the other hand, the rmse of temperature is further reduced; this may be linked to the strong temperature-dependence of CFC solubility.

The overall reduction in surface-to-deep transport leads to a slightly better representation of CFC-11 in EXP2. However, CFC-11 concentrations in the low latitude thermocline and in the northern North Pacific and around Antarctica are still too high. Interestingly, the parameters of EXP2 also yield a somewhat improved solution for the $\Delta^{14}C$ distribution in the deep Pacific. Obviously, the surface-to-deep ocean transport rates and deep ocean ventilation time scales are improved by improving the surface-to-thermocline transport rates.

In EXP3, the $\Delta^{14}C$ distribution is assimilated in addition to the temperature, salinity, and CFC-11 fields. The inclusion of $\Delta^{14}C$ in the assimilation implies less overall weight for the two water mass tracers temperature and salinity and more weight for the ventilation time scale tracers in the assimilation. The emphasis has thus shifted from water mass tracers only in EXP1 towards a 50% to 50% balance of water mass and ventilation tracers in EXP3. By including $\Delta^{14}C$ in the assimilation, we expect a more realistic representation of deep ocean ventilation compared to EXP2 and EXP1.

The most notable change in the solution is the reduction in diapycnal diffusivity by more than a factor of two in EXP3 compared to EXP2 and EXP1. The Gent–McWilliams parameter is further reduced and the freshwater flux in the North Atlantic slightly

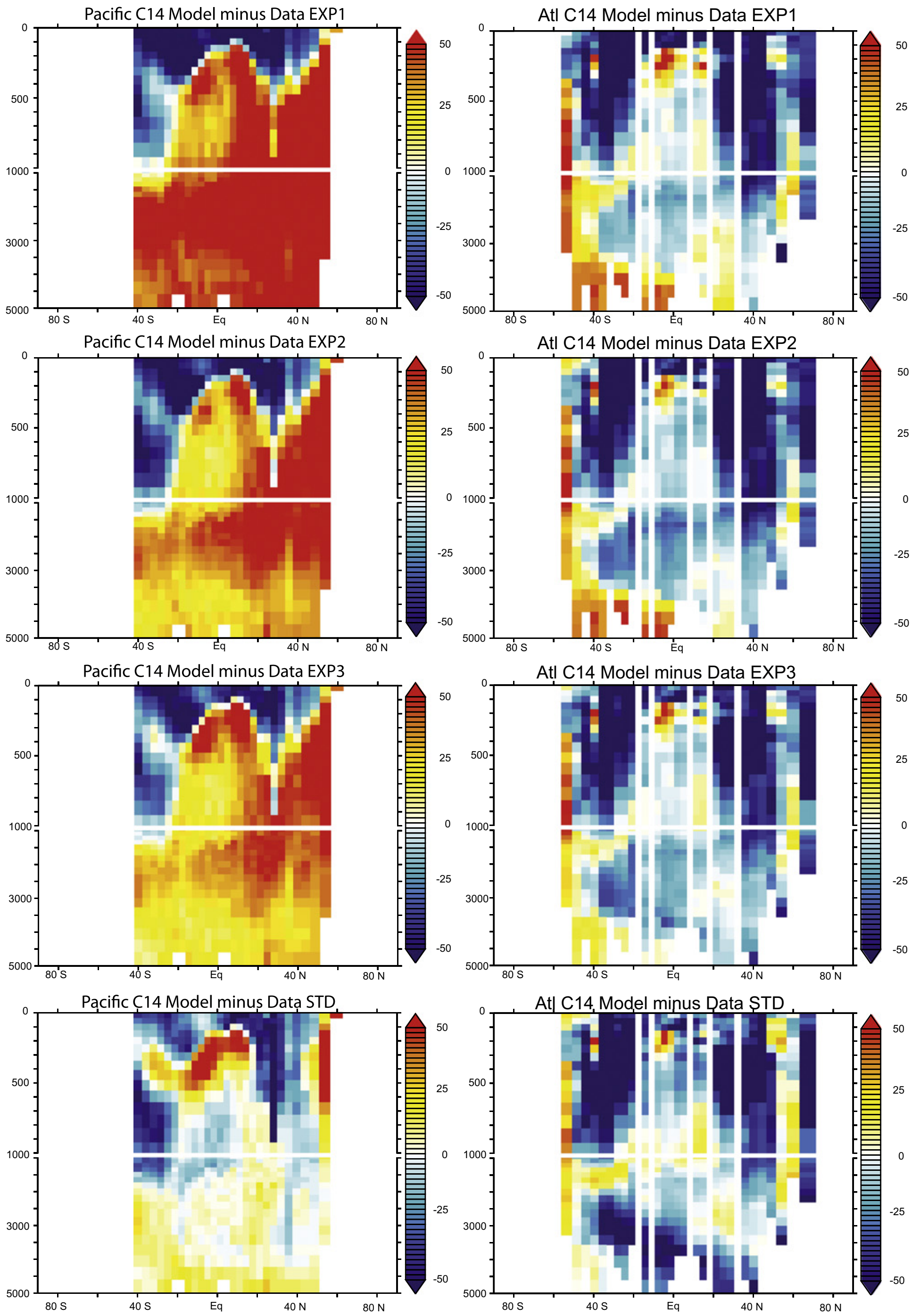

Fig. 5. $\Delta^{14}C$ residuals (model minus data, in ‰) in the Pacific (1991) and Atlantic (1972).

increased. Wind stress is somewhat higher in EXP3 than EXP2, but at the same time friction is reduced. The main effect is a reduction in the Atlantic Meriodional Overturning Circulation (AMOC) from 17 to 15 Sv and also a reduction in Southern Ocean overturning in EXP3 compared to EXP2. The reduction in AMOC is most likely linked to the decrease in the diapycnal diffusivity and the increase in friction as sensitivity simulations reveal that the AMOC scales both with diapycnal diffusivity and friction (e.g., Bryan, 1987). The penetration depth of NADW is still too deep and too little AABW is entering the deep Atlantic. Apparently, the few grid cells in the deep Atlantic that should be mainly filled by AABW do not provide a strong incentive to the filter to improve AABW formation.

The solution of EXP3 yields parameter values that are relatively close to those of the standard setup for which the parameters have been selected to match CFC-11 and radiocarbon targets. The modeled temperature and salinity distributions are very similar between the standard and the setup of EXP3. On the other hand, the penetration of CFC-11 in the equatorial thermocline is larger for EXP3 than for the standard setup and as observed whereas CFC-11 concentration are too high in the North Atlantic around 40°N in the standard. The most remarkable difference is perhaps that the radiocarbon distribution in the deep Pacific (below 1000 m) is very well represented in the standard setup, whereas values are still somewhat too high for EXP3 (Fig. 6). This shortcoming is likely linked to a too vigorous

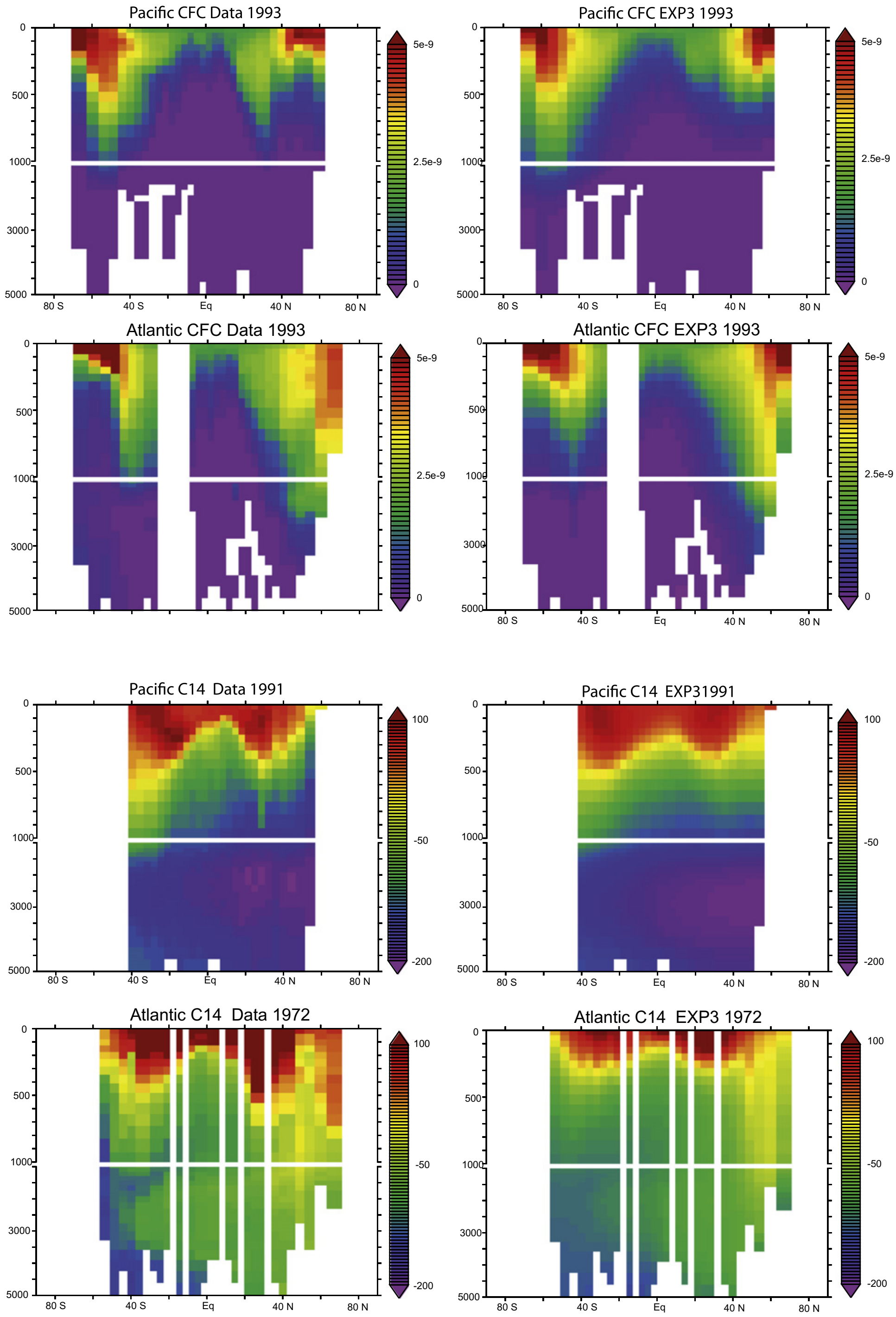

Fig. 6. Observed and modeled (EXP3) distribution of CFC-11 (in mol m^{-3}) in the Pacific and Atlantic for the year 1993 (upper part of the figure) and of $\Delta^{14}C$ (in permil) in the Pacific (1991) and Atlantic (1972) (lower part of the figure).

overturning cell in the northern North Pacific which may be linked to the enhanced the Gent–McWilliams parameter in EXP3 (Fig. 1). The Gent–McWilliams parameter and the isopycnal diffusion are quite different between EXP3 and STD, however, their contribution to the surface-to-deep transport and ventilation of the thermocline is rather limited.

Overall, our results suggest that the ventilation characteristics of the thermocline and the deep ocean are relatively poorly represented when only temperature and salinity fields are used as targets in the assimilation. The situation is improved when adding CFC-11 as a target in EXP2 and when adding radiocarbon as an additional target in EXP3 (Figs. 6 and 7).

3.2. Influence of different assimilation targets on biogeochemical tracer distributions

Next, we investigate how well the distribution of biogeochemical tracers is simulated by the three setups of EXP1, EXP2, and EXP3 and the standard. Biogeochemical tracers were not assimilated in the optimization. The parameters of the biogeochemical

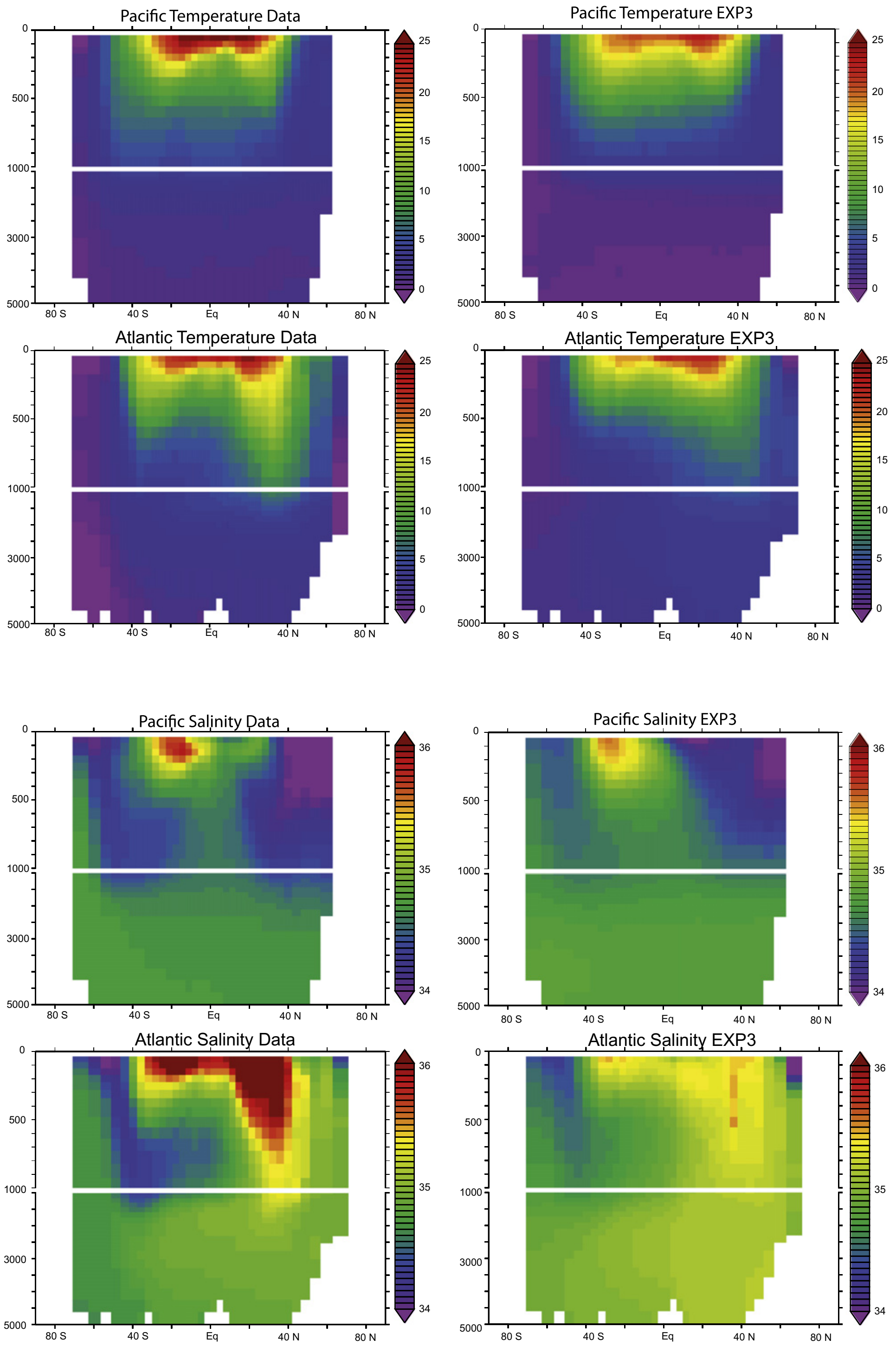

Fig. 7. Observed and modeled (EXP3) distribution of summer (JJA) temperature (in °C) in the Pacific and Atlantic (upper part of the figure) and of summer (JJA) salinity (in psu) in the Pacific and Atlantic (lower part of the figure).

module (Parekh et al., 2008; Tschumi et al., 2011) are not adjusted for the three setups. All setup feature the observed large-scale tracer gradients with nutrient concentrations increasing along the path of North Atlantic Deep Water to the Southern Ocean and with highest concentration in the northern North Pacific at mid-depth (see Figs. S1–S5).

All three EnKF setups show a low bias in PO_4, silicate and DIC and a corresponding high bias in O_2 in the North Pacific in the thermocline and down to a depth of 3000 m. Apparently, overturning and surface-to-deep exchange is too vigorous in the northern North Pacific in the setups of EXP1, EXP2, and EXP3. The standard setup shows much better agreement with the nutrient and oxygen observations, this points towards a more realistic overturning and surface-to-deep transport in STD. EXP 1 shows also a high bias in O_2 and a low bias in DIC in the Pacific sector of the Southern Ocean and the in the deep Pacific (below 3000 m). This oxygen bias is reduced in EXP2 and EXP3 and approximately removed in STD. This may be a further indication that Southern Ocean and deep Pacific ventilation is more realistic for EXP3 than EXP1.

Table 2
RMSE, correlation and relative standard deviation (relative to the standard deviation of the observation-based data) from the different EnKF-data assimilation experiments. Each grid cell is given equal weight and seasonal data for temperature and salinity are used. The consideration of monthly data instead of annual mean data and of equal weight per grid cell instead equal weight per unit volume yields usually larger deviations between observation-based fields and simulated fields.

	EXP1	EXP2	EXP3	STD
RMSE				
Temperature (°C)	1.78	1.71	1.67	1.67
Salinity (psu)	0.35	0.38	0.39	0.39
CFC-11 (mol m^{-3})	$7.15 \cdot 10^{-10}$	$6.16 \cdot 10^{-10}$	$6.48 \cdot 10^{-10}$	$6.84 \cdot 10^{-10}$
$\Delta^{14}C$ (‰)	49.82	44.09	41.25	44.97
Correlation				
Temperature	0.96	0.96	0.96	0.96
Salinity	0.72	0.66	0.66	0.66
CFC-11	0.86	0.89	0.89	0.87
$\Delta^{14}C$	0.93	0.94	0.94	0.93
Relative standard deviation				
Temperature	0.97	0.96	0.98	0.98
Salinity	0.66	0.80	0.83	0.83
CFC-11	0.94	0.94	1.	0.98
$\Delta^{14}C$	0.65	0.71	0.77	0.89

There are also biases in the other basins. Notably, nutrient concentrations are too high and oxygen is too low in the deep Atlantic in all three EnKF circulations as AABW is too weak. The standard setup matches better the nutrient distribution, however has a low bias in oxygen. In the Indian ocean, all three EnKF circulations show too high nutrient concentrations in the upper tropical ocean, and too low concentrations of nutrients in the deep ocean. The same residual pattern but to a lesser extend can be found in the standard setup.

Fig. 8 shows rmse, standard deviation, and correlation between normalized observation-based and simulated fields in a Taylor diagram for total dissolved inorganic carbon (DIC), alkalinity (ALK), oxygen (O_2), phosphate (PO_4) and silicate. EXP3 yields best results for these metrics among the three setups and for all tracers, except for ALK. The representation of ALK is poor in our model, a shortcoming shared with the current crop of biogeochemical models (Roy et al., 2011; Keller et al., 2012). The assimilation of temperature, salinity, CFC-11, and radiocarbon yields better metrics than the standard model setup for DIC, ALK and silicate and comparable numbers for PO_4, whereas oxygen is considerably less well represented in EPX3 than the standard setup. This is a consequence of the too rapid ventilation of the North Pacific due to the unrealistically strong overturning circulation in the upper North Pacific (Fig. 1). The evaluation of the biogeochemical tracers does not unambiguously favor a particular model setup also as tunable parameters of the biogeochemical module were not included in the assimilation but kept at their standard values. However, there is an indication that the standard setup and EXP3, where temperature, salinity, CFC-11, and radiocarbon field were assimilated, yield overall the best results in terms of the applied statistical metrics. However, further work, addressing also the choice of parameters of the biogeochemical module, would be required to draw firm conclusions in this respect. It is interesting to note that the standard model setup, which has been tuned to match five targets, CFC-11 inventories in the Pacific and Southern Ocean and radiocarbon signatures of NADW, Circumpolar Water and North Pacific waters, performs similar as EXP3 in terms of the statistical metrics shown in Fig. 8 and Table 2. This suggest that the results are similar whether the entire fields of CFC-11 and radiocarbon are assimilated as in EXP3 or just the mean radiocarbon signature and CFC-11 inventories of main water masses are used as targets.

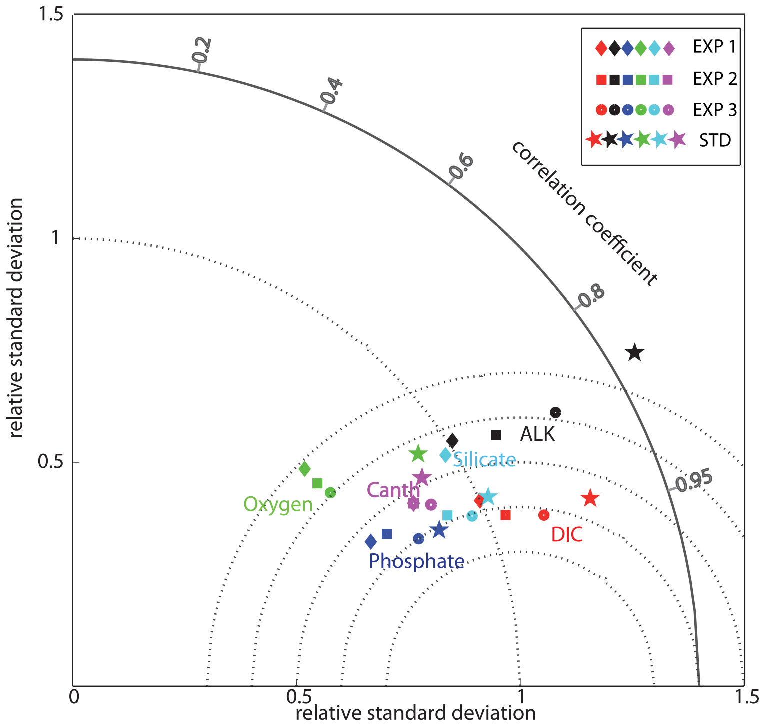

Fig. 8. Taylor diagram comparing observation-based and simulated fields of DIC, C_{anth}, alkalinity, phosphate, oxygen and silicate of the three circulation setups (EXP1, EXP2 and EXP3) and the Bern3D standard model setup (STD) (Müller et al., 2006; Ritz et al., 2011; Tschumi et al., 2010). The angular coordinate indicates the correlation coefficient (R), the radial coordinate shows the normalized standard deviation (std_{model}/std_{obs}). A model perfectly matching the observations would reside in point (1, 1). In EXP1 there is an accumulation of DIC, phosphate and alkalinity in a few bottom cells that leads to concentrations that are up to ten times too high. This is attributed to instabilities in the tracer transport with a high Gent–McWilliams mixing parameter. These few cells were excluded for the calculation of the correlation and the relative standard deviation.

3.3. Influence of different assimilation targets on carbon uptake over the industrial period and climate-carbon cycle projections

In this section, we address the question to which extent the inclusion of the ventilation time scale tracers CFC-11 and radiocarbon in the Ensemble Kalman Filter assimilation changes climate-carbon cycle projections. We investigate the influence of the different model setups on ocean carbon and heat uptake, on projected surface warming, and sea level rise and the Atlantic Meridional Overturning Circulation (AMOC). Atmospheric CO_2 is prescribed in the model to stabilize at 450 and 1000 ppm following the CO_2 stabilization profiles SP450 and SP1000, respectively (Fig. 9a) (Plattner et al., 2008). Simulations are run with the parameters as determined by the Ensemble Kalman Filter assimilation and standard model setup including the biogeochemical and ocean sediment modules and run until year 3000.

The global response is qualitatively similar across the four setups (Fig. 9). Ocean carbon uptake continues to increase, peaks around year 2080 in SP100 and around 2025 in SP450, and decreases thereafter (Fig. 9e). Atmospheric surface air temperature increases rapidly with rising CO_2 and at a much slower rate after the CO_2 concentration has been stabilized around 2100 and 2375 years in SP450 and S1000, respectively (Fig. 9b). Global ocean heat and carbon content and sea level increase throughout the simulations due to continuous uptake of heat and carbon. At year 3000, the ocean heat and carbon distribution is still away from equilibrium with the atmosphere for both CO_2 stabilization levels (Fig. 9b,c,d,f). This is a consequence of the century-to-millennial overturning time scales of the deep ocean.

The global uptake rates of CO_2 by the ocean are compared to other model studies or observation-based estimates (see Table 3). The uptake rates of the EXP3 (2.17 GtC yr^{-1} for the year 1995) compare quite well with the inverse studies of Mikaloff Fletcher et al. (2006), Gerber and Joos (2010) and the model study in Matsumoto et al. (2004) (2.20 GtC yr^{-1}). The observation-based estimate of the global uptake reported in Ishidoya et al. (2012) (2.5 GtC yr^{-1} for the year 2000–2010) is slightly lower than the 2.58 GtC yr^{-1}) of EXP3 for the corresponding period. The uptake rates for the STD setup are at the lower limit of the reported uncertainty, whereas the uptake rates of EXP1 tend to exceed both the observation-based and the model derived uptake rates of CO_2. This is a consequence of the vigorous vertical mixing in EXP1.

The 21st century uptake of CO_2 by the ocean is similar for the model setups of EXP2 and EXP3 which both show higher uptake rates than the standard setup (STD) but substantially lower than EXP1 (Fig. 9e). The inclusion of CFC-11 in the EnKF assimilation yields a less vigorous, and likely more realistic, ventilation of the thermocline compared to the temperature and salinity data assimilation of EXP1. The tuning towards radiocarbon inventories of main water masses of the ocean (Matsumoto et al., 2004) further reduces the vigorous transport to the deep ocean. The peak annual uptake rate is 3.42 GtC yr^{-1} in STD (3.99 GtC yr^{-1} in EXP3) compared to 4.72 GtC yr^{-1} in EXP1 for SP1000. Similarly, the peak uptake around year 2025 is also reduced for the low stabilization SP450 target profile from 3.59 GtC yr^{-1} in EXP1 to 2.65 GtC yr^{-1} in STD (3.07 GtC yr^{-1} in EXP3). Clearly, the inclusion CFC-11 in the data assimilation in EXP2 and radiocarbon inventories in STD

Table 3
Oceanic uptake of anthropogenic carbon (C_{anth}) for the four model setups compared to published estimates.

Study and period	Uptake in GtC yr^{-1}	EXP1	EXP2	EXP3	STD
Mikaloff Fletcher et al. (2006) 1995	2.2 ± 0.25	2.49	2.18	2.16	1.84
Gerber and Joos (2010) 1995	2.1 ± 0.3	2.49	2.18	2.16	1.84
Matsumoto et al. (2004) 1990–2000	2.2 ± 0.2	2.51	2.20	2.17	1.86
Takahashi et al. (2009) 2000	1.9 ± 0.7	2.72	2.38	2.35	2.02
Ishidoya et al. (2012) 2000–2010	2.5 ± 0.7	2.96	2.59	2.58	2.20

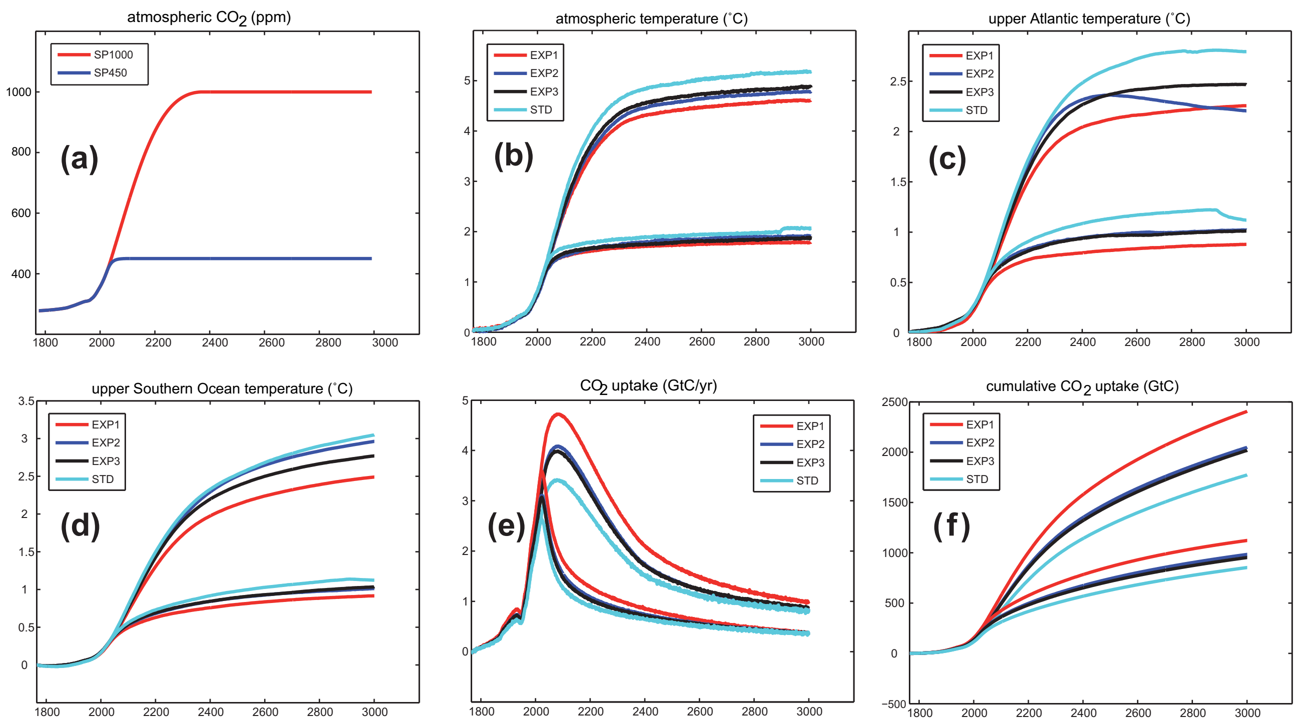

Fig. 9. (a) Prescribed atmospheric CO_2 following the SP450 and SP1000 stabilization profiles, and projected increase (b) in global mean atmospheric surface temperature (c) in upper (above 1000 m depth) Atlantic and (d) upper Southern Ocean temperature, and (e) annual and (f) cumulative air-to-sea carbon flux.

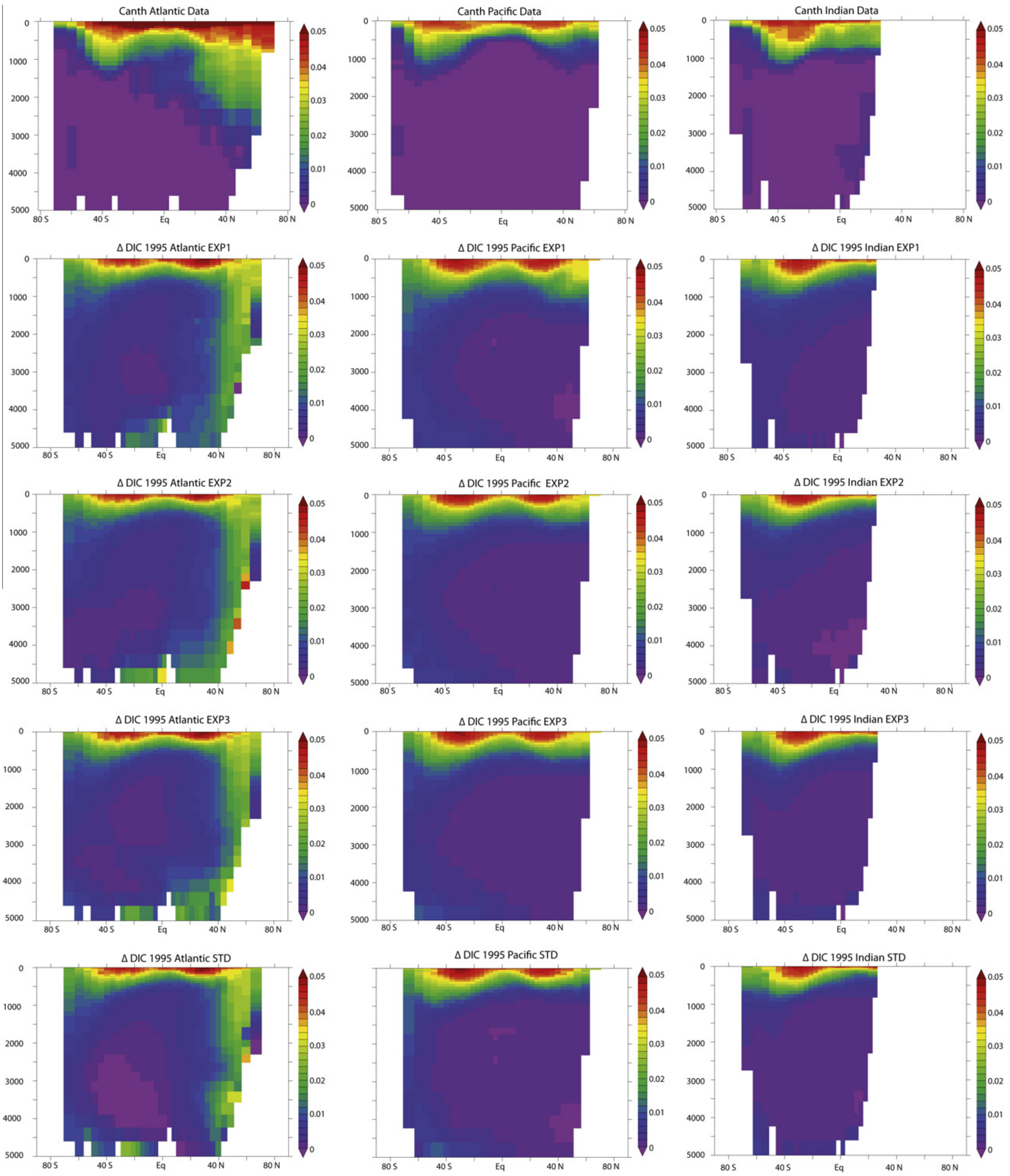

Fig. 10. Data-based distribution of C_{anth} (Key et al., 2004) and simulated changes in the concentration of dissolved inorganic carbon (DIC; mol m^{-3}) for the four model setups and by year 1994. Top to bottom: data-based C_{anth}, EXP1, EXP2, EXP3 and standard setup; left to right: Atlantic, Pacific and Indian Ocean.

and EXP3 yields a considerably lower allowance for anthropogenic carbon emissions to meet a certain CO_2 stabilization concentration.

The difference in ocean carbon uptake flux continues until the end of the simulations in year 3000. In SP1000, the cumulative uptake by year 3000 is 2406 GtC in EXP1 almost 35% higher than in STD (1774 GtC) (Fig. 9f) and and still about 20% higher than in EXP3 (2019 GtC). Similarly for SP450, the total uptake of 853 GtC for the STD setup is 270 GtC or 24% lower than for EXP1.

The spatial pattern of the change in the concentration of dissolved inorganic carbon, Δ DIC, reveals some common features across all setups and some remarkable differences (Figs. 10 and 11). The global pattern of Δ DIC in the year 1994 compares quite well to the observation-based estimates of C_{anth} (Key et al., 2004) for all four setups (see Fig. 10). The anthropogenic signal decreases from the surface through the thermocline and penetrates the deep ocean only in the North Atlantic through the NADW pathway.

The reconstruction method to quantify C_{anth} relies on various assumptions such as constant Redfield ratios and does in general not account for changes in the biogeochemistry related to changes in ocean circulation and for carbon fluxes at the sediment-ocean interface in the deep ocean. In contrast, these processes are included in the Bern3D model and affect simulated changes in Δ DIC in the deep Southern Pacific and the deep Atlantic. We also note that alternative reconstruction methods yield higher C_{anth} values in the Southern Ocean (Rodríguez et al., 2009; Álvarez et al., 2009) than the method applied for the GLODAP data (Key et al., 2004).

The RMSE between Δ DIC and the observation-based estimates of C_{anth} are between 7.6 μmol/kg (EXP3) and 8.8 μmol/kg (STD), which is in the range of the uncertainty of the reconstruction methods of C_{anth} (e.g., Gruber et al., 1996; Khatiwala et al., 2012). The correlation is between 0.86 (STD) and 0.89 (EXP3), the relative standard deviation between 0.87 (EXP1 and EXP2) and 0.91 (STD) (see Fig. 8). The good agreement between the modeled uptake rates of C_{anth} (Table 3) and the reasonably low deviation between modeled Δ DIC and observation-based C_{anth} shows that the model is able to capture the large-scale pathways of ocean circulation and surface-to-deep overturning time scales.

Next we discuss the patterns for the SP1000 profile and at the end of the simulation at year 3000. The higher Δ DIC concentration are found in low and mid-latitude surface waters than in polar surface waters. This is explained by the larger C uptake capacity in response to an increase in atmospheric CO_2 (Revelle factor) for warm compared to cold water. Similar Δ DIC concentrations as in the polar surface water (source region) are simulated at mid depth in the Atlantic, the Southern and Indian Ocean and the South Pacific. Lowest changes in DIC are simulated in the northern North Pacific where radiocarbon ventilation ages are the lowest of the entire ocean.

Ocean–sediment interactions yield high Δ DIC values where NADW reaches the ocean bottom in the deep Atlantic as well as in the deep Southern Pacific and deep Indian. The uptake of the weak acid CO_2 causes a lowering of ocean pH by 0.4 units on global average and for SP1000 by 3000 AD. The reduction in pH changes the saturation state of water with respect to calcite towards less saturated conditions towards less saturated conditions (we note that calcium carbonate in the form of aragonite or high-magnesium calcite is not included in the model). In turn, the saturation horizon separating oversaturated from undersaturated water is rising and more calcite dissolves from the sediments causing DIC, and also pH and alkalinity, of the overlying water to increase. The contribution from the sediments and from changes in the weathering/burial balance to the DIC changes is 85 GtC (STD), 152 GtC (EXP3),

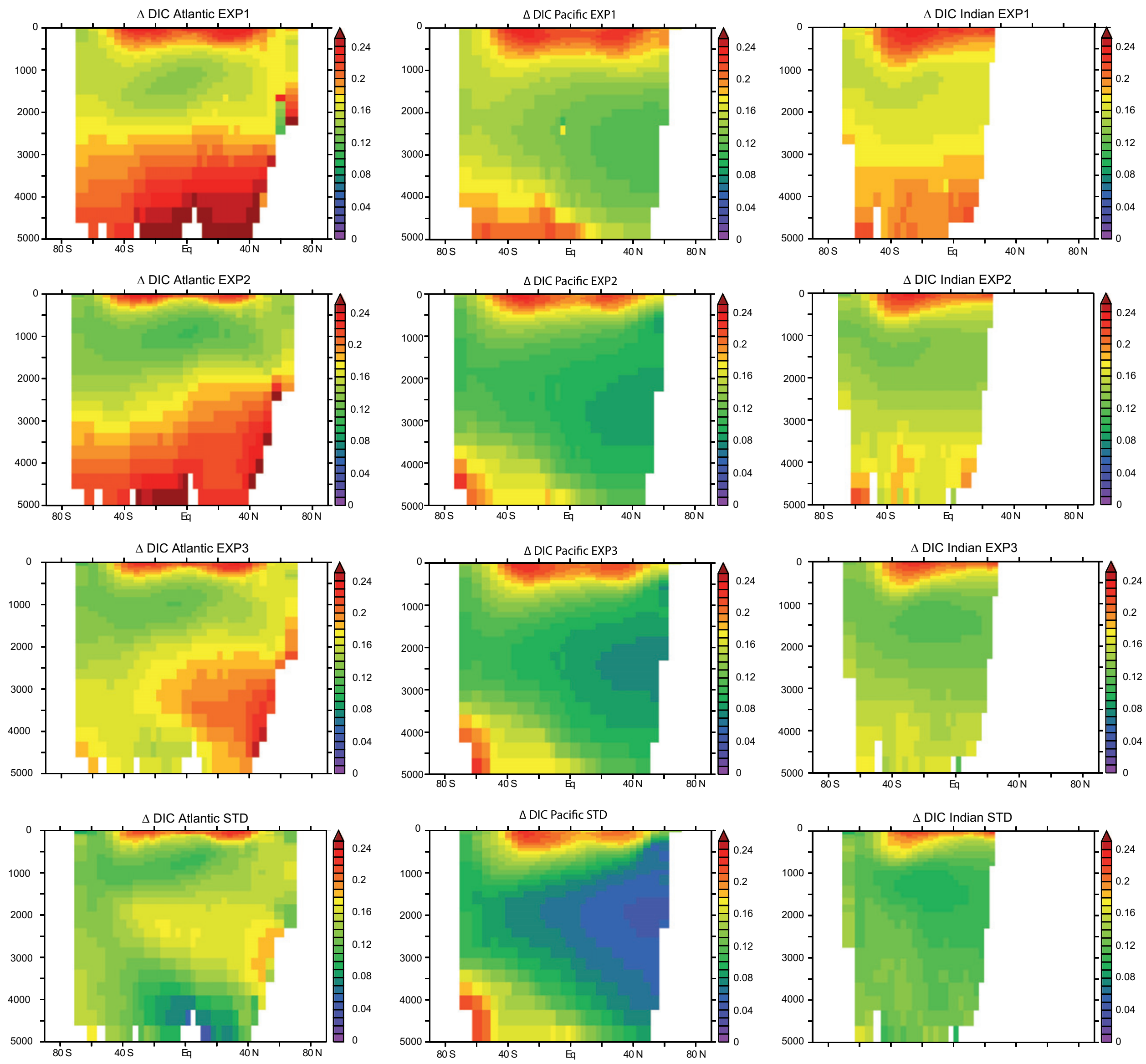

Fig. 11. Projected changes in the concentration of dissolved inorganic carbon (mol m^{-3}) for the four model setups. Results are for year 3000 AD and the SP1000 stabilization profile where atmospheric CO_2 is prescribed to stabilize at 1000 ppmv. Top to bottom: EXP1, EXP2, EXP3 and standard setup; left to right: Atlantic, Pacific and Indian Ocean.

Table 4
Increase in global mean surface air temperature (ΔT_{atm}), global ocean temperature ($\Delta T_{g.O}$) and upper Southern Ocean temperature ($\Delta T_{S.O.}$) in °C and steric sea-level rise (SSLR) in meters under the SP1000 scenario for the four model setups.

	ΔT_{atm} at 2100	ΔT_{atm} at 3000	$\Delta T_{g.O.}$ at 3000	$\Delta T_{S.O.}$ at 3000	SSLR at 3000
EXP1	2.41	4.6	1.85	2.49	1.04
EXP2	2.50	4.79	1.82	2.97	0.96
EXP3	2.52	4.9	1.78	2.77	0.92
STD	2.67	5.07	1.88	3.05	0.97

201 GtC (EXP2) and 254 GtC (EXP1) by year 3000. This contribution is less than 10% of the whole ocean DIC change.

The four setups result in distinct distributions of Δ DIC (Fig. 11). The higher ventilation rate of the deep ocean of EXP1 and EXP2 compared to EXP3 and STD result also in considerably larger Δ DIC concentrations in the deep ocean. The high formation rate and deep penetration of NADW in EXP1 and EXP2 yield, in combination with ocean-sediment interactions, much higher Δ DIC concentrations in the deep Atlantic than for EXP3 and the standard configuration (STD). The EnKF-inferred circulations (EXP1, EXP2 and EXP3) show a much stronger increase in DIC in the North Pacific compared to the standard setup, apparently a result of the too vigorous surface-to-deep mixing in the northern North Pacific.

The projected climate change depends on the radiative forcing of the prescribed atmospheric CO_2 and the amplification by climate feedbacks such as those related to water vapor or snow and ice coverage and on the ventilation time scales governing ocean heat uptake. Table 4 shows differences in projected climate variables for the different model setups. The differences in global mean surface warming, ocean heat content, and steric sea level rise of up to 15% are notable, but small compared to uncertainties in the climate sensitivity of about a factor of two.

Differences among model setup also emerge for the distribution of additional heat within the ocean and for changes in ocean circulation. For example, the mean temperature increase in the upper 1000 m of the Southern ocean (Fig. 7d) ranges between 2.49 (EXP1) and 3.05 °C (STD) for SP1000 and year 3000. Such differences in surface warming could be highly relevant for the fate of the Antarctic Ice Sheet as ice melting due to warm water has the potential to affect ice sheet stability.

The global warming leads to a stratification of the ocean, which reduces the strength of the Atlantic Meridional Overturning Circulation (AMOC). Under the SP1000 forcing, we find a reduction of the AMOC of about 7 Sverdrup (1 Sv = 10^6 m^3 s^{-1} in the EXP2 setup, of 6 Sv in the STD and of 5 Sv for EXP1 and EXP3. In the SP450 scenario, the AMOC is reduced by 2.5–3 Sv in the three setups. The strong reduction of NADW formation and the related reduction in meridional heat transport into the North Atlantic surface affect the temperature of the upper Atlantic. In EXP2, despite a continued increase in global-mean surface temperature, the temperature of the upper Atlantic (above 1000 m) peaks at 2.35 °C around 2400 AD and declines thereafter by 0.15 °C. until 3000 AD. Such differences in surface water temperature and related differences in air temperature may be relevant for the fate of the Greenland ice sheets and for the climate in Europe.

4. Discussion and conclusion

We applied an Ensemble Kalman Filter (EnKF) to assimilate 3-dimensional fields of temperature, salinity, CFC-11, and radiocarbon data in various combinations into the Bern3D ocean model. The purpose is to determine optimal model parameters in an objective statistical framework to improve climate-carbon cycle projections. Although,the choice of the target metric remains a subjective one. The different optimal parameter sets from the assimilations were used to simulate the distribution of a range of biogeochemical tracers and to project changes in the carbon cycle and in climate for CO_2 stabilization pathways. A caveat that applies to this work is that the Bern3D model is of coarse horizontal resolution and it features a simplified geostrophic-frictional balance dynamics.

The assimilation of temperature and salinity fields does not yield satisfactory results in terms of surface-to-deep transport. Ventilation of the thermocline and the deep ocean becomes too vigorous in the Bern3D model as evidenced by high CFC-11 inventories and high radiocarbon signatures. The inclusion of CFC-11 as an additional target in the assimilation yields a better representation of the mixing time scales of the thermocline as well as of the deep ocean and the inclusion of radiocarbon promotes the formation of Antarctic Bottom Water.

The use of the two water mass tracers (salinity and temperature) and the two ventilation tracers (CFC-11 and radiocarbon) as targets yields overall the best results for biogeochemical tracers among the different EnKF solutions. However, the parameters of the biogeochemical module have not been tuned together with the physical model parameters and there remains the possibility that a suitable combination of transport and biogeochemical parameters might even lead to a better representation of biogeochemical tracer fields. Nevertheless, the statistics for the physical tracers and the biogeochemical tracers (Table 2 and Fig. 8) may suggest that the assimilation of CFC-11 and radiocarbon data improves overall model performance as compared to the assimilation of temperature and salinity only. This appears to support the use of all four tracer fields as targets.

The standard setup of the Bern3D ocean model and the setup from the assimilation with all four tracer fields yield similar results in terms of simulated tracer distributions (Figs. 2–5) and statistical metrics (Table 2). The standard version has been tuned by matching five targets (Müller et al., 2006). The assimilation of 3-d tracer fields does not necessarily lead to an improvement compared to a model which has been tuned with large-scale inventories as targets (e.g., Matsumoto et al., 2004).

However, there remain differences in simulated ocean carbon uptake rates and surface warming between these setups. These appear to be related to the details how the information provided by CFC-11 and radiocarbon observations is used for parameter determination. The Gent–McWilliams, isopycnal and diapycnal diffusivities are higher in EXP3 than in the STD setup. This yields a somewhat more vigorous surface-to-deep transport in EXP3 compared to the standard setup. Carbon uptake rates for the standard setup are at the lower end compared to data-based estimates (Table 3), suggesting that the transport of excess carbon to the abyss is perhaps somewhat too sluggish. The carbon uptake rates obtained with EXP3 are close to the central estimates of Mikaloff Fletcher et al. (2006), Gerber and Joos (2010), Matsumoto et al. (2004), Ishidoya et al. (2012) (Table 3). The sensitivity of the model solution in terms of simulated tracer fields to variations in the GM and isopycnal diffusivities appears relatively low; this is indicated by the large difference in these parameter values for EXP3 and STD (Table 1), despite their similar error statistics (Table 2).

In conclusion, we applied a cost-efficient dynamic ocean model that allowed us to test different combinations of assimilation targets. Our results suggest that temperature, salinity, CFC-11, and radiocarbon observations should be included as targets in future ocean model optimization studies.

Acknowledgements

We thank the reviewers for their critical and constructive comments that helped to improve this manuscript. We acknowledge

Martin Schneiter for his help to run the model. This project was funded by the EU FP7 project CARBOCHANGE Changes in carbon uptake and emissions by oceans in a changing climate which received funding from the European Community's Seventh Framework Programme under Grant Agreement No. 264879 and by the Swiss National Science Foundation.

Appendix A. Supplementary data

Supplementary data associated with this article can be found, in the online version, at http://dx.doi.org/10.1016/j.ocemod.2012.12.012.

References

Álvarez, M., Lo Monaco, C., Tanhua, T., Yool, A., Oschlies, A., Bullister, J.L., Goyet, C., Metzl, N., Touratier, F., McDonagh, E., Bryden, H.L., 2009. Estimating the storage of anthropogenic carbon in the subtropical indian ocean: a comparison of five different approaches. Biogeosciences Discussion 6 (1), 729–796.

Annan, J.D., Hargreaves, J.C., Edwards, N.R., Marsh, R., 2005. Parameter estimation in an intermediate complexity earth system model using an ensemble Kalman filter. Ocean Modelling 8 (1-2), 135–154.

Antonov, J.I., Seidov, D., Boyer, T.P., Locarnini, R.A., Mishonov, A.V., Garcia, H.E., Baranova, O.K., Zweng, M.M., Johnson, D.R., 2010. Vol. 2: Salinity. In: Levitus, S. (Ed.), World Ocean Atlas 2009. NOAA Atlas NESDIS 69. U.S. Government Printing Office, Washington, D.C., 184 pp.

Bhat, K.S., Haran, M., Olson, R., Keller, K., 2012. Inferring likelihoods and climate system characteristics from climate models and multiple tracers. Environmetrics 23, 345–362.

Boé, J., Hall, A., Qu, X., 2009. Deep ocean heat uptake as a major source of spread in transient climate change simulations. Geophysical Research Letters 36, L22701.

Bryan, F., 1987. Parameter sensitivity of primitive equation ocean general circulation models. Journal of Physical Oceanography 17 (7), 970–985.

Cao, L., Eby, M., Ridgwell, A., Caldeira, K., Archer, D., Ishida, A., Joos, F., Matsumoto, K., Mikolajewicz, U., Mouchet, A., Orr, J.C., Plattner, G.-K., Schlitzer, R., Tokos, K., Totterdell, I., Tschumi, T., Yamanaka, Y., Yool, A., 2009. The role of ocean transport in the uptake of anthropogenic CO_2. Biogeosciences 6 (3), 375–390.

Doney, S.C., Glover, D.M., Najjar, R.G., 1996. A new coupled, one-dimensional biological-physical model for the upper ocean: Applications to the JGOFS Bermuda Atlantic time-series study (BATS) site 1. Deep Sea Research, Part II 43, 591624.

Doney, S.C., Lindsay, K., Caldeira, K., Campin, J.-M., Drange, H., Dutay, J.-C., Follows, M., Gao, Y., Gnanadesikan, A., Gruber, N., Ishida, A., Joos, F., Madec, G., Maier-Reimer, E., Marshall, J.C., Matear, R.J., Monfray, P., Mouchet, A., Najjar, R., Orr, J.C., Plattner, G.-K., Sarmiento, J., Schlitzer, R., Slater, R., Totterdell, I.J., Weirig, M.-F., Yamanaka, Y., Yool, A., 2004. Evaluating global ocean carbon models: the importance of realistic physics. Global Biogeochemical Cycles 18, GB3017.

Edwards, N.R., Marsh, R., 2005. Uncertainties due to transport-parameter sensitivity in an efficient 3-d ocean-climate model. Climate Dynamics 24 (4), 415–433.

England, M.H., Maier-Reimer, E., 2001. Using chemical tracers to assess ocean models. Reviews of Geophysics 39 (1), 2970.

Evensen, G., 2003. The Ensemble Kalman Filter: theoretical formulation and practical implementation. Ocean Dynamics 53, 343–367.

Friedlingstein, P., Dufresne, J.L., Cox, P.M., Rayner, P., 2003. How positive is the feedback between climate change and the carbon cycle? Tellus 55B, 692700.

Frölicher, T.L., Joos, F., 2010. Reversible and irreversible impacts of greenhouse gas emissions in multi-century projections with the NCAR global coupled carbon cycle-climate model. Climate Dynamics 35 (7-8), 1439–1459.

Ganachaud, A., Wunsch, C., 2000. Improved estimates of global ocean circulation, heat transport and mixing from hydrographic data. Nature 408, 453 457.

Gangstø, R., Joos, F., Gehlen, M., 2011. Sensitivity of pelagic calcification to ocean acidification. Biogeosciences 8 (2), 433–458.

Gehlen, M., Bopp, L., Emprin, N., Aumont, O., Heinze, C., Ragueneau, O., 2006. Reconciling surface ocean productivity export fluxes and sediment composition in a global biogeochemical ocean model. Biogeosciences 3, 521537.

Gent, P.R., Willebrand, J., McDougall, T.J., McWilliams, J.C., 1995. Parameterizing eddy-induced tracer transports in ocean circulation models. Journal of Physical Oceanography 25, 463–474.

Gerber, M., Joos, F., 2010. Carbon sources and sinks from an Ensemble Kalman Filter ocean data assimilation. Global Biogeochemical Cycles 24, GB3004.

Gerber, M., Joos, F., Vázquez Rodríguez, M., Touratier, F., Goyet, C., 2009. Regional air-sea fluxes of anthropogenic carbon inferred with an Ensemble Kalman Filter. Global Biogeochemical Cycles 23, GB1013.

Goes, M., Urban, N.M., Tonkonojenkov, R., Haran, M., Schmittner, A., Keller, K., 2010. What is the skill of ocean tracers in reducing uncertainties about ocean diapycnal mixing and projections of the Atlantic Meridional Overturning Circulation? Journal of Geophysical Research 115, C12006.

Gregory, J.M., Mitchell, J.F.B., 1997. the climate response to CO_2 of the Hadley Centre coupled AOGCM with and without flux adjustment. Geophysical Research Letters 24 (15), 19431946.

Griffies, S.M., 1998. The Gent-McWilliams skew flux. Journal of Physical Oceanography 28 (5), 831–841.

Gruber, N., Sarmiento, J., Stocker, T.F., 1996. An improved method for detecting anthropogenic CO_2 in the oceans. Global Biogeochemical Cycles 10 (4), 809–837.

Hargreaves, J.C., Annan, J.D., Edwards, N.R., Marsh, R., 2004. An efficient climate forecasting method using an intermediate complexity Earth System Model and the ensemble Kalman filter. Climate Dynamics 23 (7-8).

Heinze, C., Maier-Reimer, E., Winguth, A.M.E., Archer, D., 1999. A global oceanic sediment model for long-term climate studies. Global Biogeochemical Cycles 13, 221–250.

Ishidoya, S., Aoki, S., Goto, D., Nakazawa, T., Taguchi, S., Patra, P.K., 2012. Time and space variations of the O_2/N_2 ratio in the troposphere over japan and estimation of the global CO_2 budget for the period 2000–2010. Tellus B 64 (18964), 463–474.

Joos, F., Plattner, G.-K., Stocker, T.F., Marchal, O., Schmittner, A., 1999. Global warming and marine carbon cycle feedbacks on future atmospheric CO_2. Science 284 (5413), 464–467.

Joos, F., Siegenthaler, U., Sarmiento, J., 1991. Possible effects of iron fertilization in the southern ocean on atmospheric CO_2 concentration. Global Biogeochemical Cycles 5 (2), 135–150.

Kalnay, E., Kanamitsu, M., Kistler, R., Collins, W., Deaven, D., Gandin, L., Iredell, M., Saha, S., White, G., Woollen, J., Zhu, Y., Leetma, A., Reynolds, R., Chelliah, M., Ebisuzaki, W., Higgins, W., Janowiak, J., Mo, K.C., Ropelewski, C., Wang, J., Jenne, R., Joseph, D., 1996. The ncep/ncar 40-year reanalysis project. Bulletin of the American Meterorological Society 77 (3), 437–471.

Keller, K.M., Joos, F., Raible, C.C., Cocco, V., Frölicher, T.L., Dunne, J.P., Gehlen, M., Roy, T., Bopp, L., Orr, J.C., Tjiputra, J., Heinze, C., Segschneider, J., Metzl, N., 2012. Variability of the ocean carbon cycle in response to the North Atlantic oscillation. Tellus B, 64/18738.

Key, R.M., Kozyr, A., Sabine, C.L., Lee, K., Wanninkhof, R., Bullister, J.L., Feely, R.A., Millero, F.J., Mordy, C., Peng, T.-H., 2004. A global ocean carbon climatology: results from Global Data Analysis Project (GLODAP). Global Biogeochemical Cycles 18, GB4031.

Khatiwala, S., Tanhua, T., Mikaloff Fletcher, S., Gerber, M., Doney, S.C., Graven, H.D., Gruber, N., McKinley, G.A., Murata, A., Ríos, A.F., Sabine, C.L., Sarmiento, J.L., 2012. Global ocean storage of anthropogenic carbon. Biogeosciences Discussion 9 (7), 8931–8988.

Levitus, S., Boyer, T., 1994. Temperature, vol. 4. In: World Ocean Atlas. 4. NOAA Atlas NESDIS, 117 pp.

Levitus, S., Burgett, R., Boyer, T., 1994. Salinity, vol. 3. In: World Ocean Atlas. 3. NOAA Atlas NESDIS, 99 pp.

Lisæter, K.A., Rosanova, J., Evensen, G., 2003. Assimilation of ice concentration in a coupled iceocean model, using the Ensemble Kalman filter. Ocean Dynamics 53 (4), 368–388.

Locarnini, R.A., Mishonov, A.V., Antonov, J.I., Boyer, T.P., Garcia, H.E., Baranova, O.K., Zweng, M.M., Johnson, D.R., 2010. Temperature, vol. 1. In: Levitus, S. (Ed.), World Ocean Atlas 2009. Ed. NOAA Atlas NESDIS 68. U.S. Government Printing Office, Washington, D.C., 184 pp.

Maier-Reimer, E., Kriest, I., Segschneider, J., Wetzel, P., 2005. The Hamburg Ocean Carbon Cycle Model HAMOCC5.1.-Technical Description Release 1.1. Tech. Rep. 14. Max Planck Inst. for Meteorol., Hamburg, Germany.

Matsumoto, K., Sarmiento, J.L., Key, R.M., Aumont, O., Bullister, J.L., Caldeira, K., Campin, J.-M., Doney, S.C., Drange, H., Dutay, J.-C., Follows, M., Gao, Y., Gnanadesikan, A., Gruber, N., Ishida, A., Joos, F., Lindsay, K., Maier-Reimer, E., Marshall, J.C., Matear, R.J., Monfray, P., Najjar, R., Plattner, G.-K., Schlitzer, R., Slater, R., Swathi, P.S., Totterdell, I.J., Weirig, M.-F., Yamanaka, Y., Yool, A., Orr, J.C., 2004. Evaluation of ocean carbon cycle models with data-based metrics. Geophysical Research Letters 31, L07303.

Meinshausen, M., Meinshausen, N., Hare, W., Raper, S.C.B., Frieler, K., Knutti, R., Frame, D.J., Allen, M.R., 2009. Greenhouse-gas emission targets for limiting global warming to 2 °C. Nature 458 (7242), 1158–1162.

Mikaloff Fletcher, S.E., Gruber, N., Jacobson, A.R., Doney, S.C., Dutkiewicz, S., Gerber, M., Follows, M., Joos, F., Lindsay, K., Menemenlis, D., Mouchet, A., Müller, S.A., Sarmiento, J.L., 2006. Inverse estimates of anthropogenic CO_2 uptake, transport, and storage by the ocean. Global Biogeochemical Cycles 20, GB2002.

Mikaloff Fletcher, S.E., Gruber, N., Jacobson, A.R., Gloor, M., Doney, S.C., Dutkiewicz, S., Gerber, M., Follows, M., Joos, F., Lindsay, K., Menemenlis, D., Mouchet, A., Müller, S.A., Sarmiento, J.L., 2007. Inverse estimate of the oceanic sources and sinks of natural CO_2 and the implied oceanic carbon transport. Global Biogeochemical Cycles 21, GB1010.

Müller, S.A., Joos, F., Edwards, N.R., Stocker, T.F., 2006. Water mass distribution and ventilation time scales in a cost-efficient, three-dimensional ocean model. Journal of Climate 19 (21), 5479–5499.

Munk, H.W., 1966. Abyssal recipe. Deep-Sea Research 13, 707–730.

Najjar, R.G., Jin, X., Louanchi, F., Aumont, O., Caldeira, K., Doney, S.C., Dutay, J.-C., Follows, M., Gruber, N., Joos, F., Lindsay, K., Maier-Reimer, E., Matear, R.J., Matsumoto, K., Mouchet, A., Orr, J.C., Sarmiento, J.L., Schlitzer, R., Weirig, M.F., Yamanaka, Y., Yool, A., 2007. Impact of circulation on export production, dissolved organic matter, and dissolved oxygen in the ocean: results from phase II of the Ocean Carbon-cycle Model Intercomparison Project (OCMIP-2). Global Biogeochemical Cycles 21, GB3007.

Natvik, L.J., Evensen, G., 2003. Assimilation of ocean colour data into a biochemical model of the North Atlantic: Part 1. Data assimilation experiments. Journal of Marine Systems, 127–153.

Oeschger, H., Siegenthaler, U., Schotterer, U., Gugelmann, A., 1975. A box diffusion model to study the carbon dioxide exchange in nature. Tellus 27 (2), 168–192.

Parekh, P., Joos, F., Müller, S.A., 2008. A modeling assessment of the interplay between aeolian iron fluxes and iron-binding ligands in controlling carbon dioxide fluctuations during Antarctic warm events. Paleoceanography 23, PA4202.

Plattner, G.-K., Knutti, R., Joos, F., Stocker, T.F., von Bloh, W., Brovkin, V., Cameron, D., Driesschaert, E., Dutkiewiz, S., Eby, M., Edwards, N.R., Fichefet, T., Hargreaves, J.C., Jones, C.D., Loutre, M.F., Matthews, H.D., Mouchet, A., Muller, S.A., Nawrath, S., Price, A., Sokolov, A., Strassmann, K.M., Weaver, A.J., 2008. Long-term climate commitments projected with climate-carbon cycle models. Journal of Climate 21 (12), 2721–2751.

Revelle, R., Suess, H.E., 1957. Carbon dioxide exchange between atmosphere and ocean and the question of an increase of atmospheric CO_2 during the past decades. Tellus 9, 18–27.

Ritz, S.P., Stocker, T.F., Joos, F., 2011. A coupled dynamical oceanenergy balance atmosphere model for paleoclimate studies. Journal of Climate 24 (2), 349–375.

Roy, T., Bopp, L., Gehlen, M., Schneider, B., Cadule, P., Frölicher, T.L., Segschneider, J., Tjiputra, J., Heinze, C., Joos, F., 2011. Regional impacts of climate change and atmospheric CO_2 on future ocean carbon uptake: a multi-model linear feedback analysis. Journal of Climate 24, 2300–2318.

Russell, J.L., Dixon, K.W., Gnanadesikan, A., Stouffer, R.J., Toggweiler, J.R., 2006. The Southern Hemisphere Westerlies in a warming world: propping open the door to the deep ocean. Journal of Climate 19 (24), 6382–6390.

Schlitzer, R., 2000. Applying the adjoint method for biogeochemical modeling: export of particulate organic matter in the world ocean. In: Kasibhata, P. (Ed.), Inverse Methods in Global Biogeochemical Cycles, AGU Monograph, pp. 107–124.

Schlitzer, R., 2002. Carbon export fluxes in the Southern Ocean: results from inverse modeling and comparison with satellite-based estimates. Deep Sea Research Part II 49, 1623–1644.

Schlitzer, R., 2007. Assimilation of radiocarbon and chlorofluorocarbon data to constrain deep and bottom water transports in the world ocean. Journal of Physical Oceanography 37 (2), 259–276.

Schmittner, A., Urban, N.M., Keller, K., Matthews, D., 2009. Using tracer observations to reduce the uncertainty of ocean diapycnal mixing and climatecarbon cycle projections. Global Biogeochemical Cycles 23, GB4009.

Takahashi, T. et al., 2009. Climatological mean and decadal changes in surface ocean pCO_2, and net sea–air CO_2 flux over the global oceans. Deep Sea Research II 10 (8–10), 554–577.

Taylor, K.E., 2001. Summarizing multiple aspects of model performance in a single diagram. Journal of Geophysical Research 106 (D7), 7183–7192.

Tschumi, T., Joos, F., Gehlen, M., Heinze, C., 2010. Deep ocean ventilation, carbon isotopes, marine sedimentation and the deglacial CO_2 rise. Climate of the Past Discussion 6 (5), 1895–1958.

Tschumi, T., Joos, F., Gehlen, M., Heinze, C., 2011. Deep ocean ventilation, carbon isotopes, marine sedimentation and the deglacial CO_2 rise. Climate of the Past 7, 771–800.

Tschumi, T., Joos, F., Parekh, P., 2008. How important are Southern Hemisphere wind changes for low glacial carbon dioxide? A model study. Paleoceanography 23, PA4208.

Vázquez Rodríguez, M., Touratier, F., LoMonaco, C., Waugh, D.W., Padin, X.A., Bellerby, R.J., Goyet, C., Metzel, N., Ríos, A.F., Perez, F.F., 2009. Anthropogenic carbon distributions in the Atlantic Ocean: data-based estimates from the Arctic to the Antarctic. Biogeosciences 6, 439–451.

Wanninkhof, R., 1992. Relationship between wind speed and gas exchange over the ocean. Journal of Geophysical Research 97, 7373–7382.